Vertical Mixing and Transports through a Stratified Shear Layer

E. J. STRANG AND H. J. S. FERNANDO

Environmental Fluid Dynamics Program, Department of Mechanical and Aerospace Engineering, Arizona State University, Tempe, Arizona

(Manuscript received 6 April 1999, in final form 20 September 2000)

ABSTRACT

A stratified shear layer was generated in the laboratory by driving a turbulent mixed layer of depth D over a quiescent, deep dense layer. As a result, a density interface of thickness δ_b across which the buoyancy jump is Δb was formed between the upper and lower layers. This density interface was embedded in a velocity shear layer of thickness δ_s across which the velocity jump was ΔU. Detailed velocity, density, and average local Richardson number ($\overline{\mathrm{Ri}}_g$) measurements were made through the stratified shear layer, from which the fluxes of momentum and density through the interface as well as energetics of the stratified shear layer were evaluated as a function of $\overline{\mathrm{Ri}}_g$. The quantities measured included the flux Richardson number ($\overline{\mathrm{Ri}}_f$), the dissipation flux coefficient ($\overline{\Gamma}$), and the eddy diffusivities of momentum and density ($\overline{K}_m$ and $\overline{K}_\rho$), averaged across the shear layer. The results were compared with various deep and coastal oceanic data as well as common oceanic eddy diffusivity and flux parameterization schemes.

1. Introduction

In a companion paper (Strang and Fernando 2001; henceforth SF01), the authors presented detailed measurements on the deepening of a turbulent mixed layer into a quiescent heavier layer using the flow configuration shown in Fig. 1a. The upper turbulent layer of mean depth D with far-field mean velocity U_m, mean density ρ_m, rms turbulent velocity u_o and integral length scale L_o was separated from the lower nonturbulent layer of buoyancy frequency N by a density interfacial layer (or pycnocline) that has a buoyancy jump Δb and thickness δ_b. As schematized in Fig. 1a, the shear layer thickness δ_s was larger than δ_b (typically $\delta_s/\delta_b > 2$), spreading across the pycnocline, with a velocity jump of ΔU, and protruding into both the upper and lower layers. Moreover, the shear layer center was slightly offset from the center of the density interface, leading to asymmetric flow structures in the interface.

The mean velocity $\overline{U}(z)$ and density $\overline{\rho}(z)$ distributions in the pycnocline area constituted a stratified shear layer, which would become unstable and degenerate sporadically to form regions of turbulent mixing. The accompanying reduction of interfacial stratification facilitated the transport of locally mixed fluid into the upper layer by turbulent eddies. In general, however, the turbulent eddies were too feeble (i.e., $\Delta b \gg u_o^2/L_o$) to scour and lift interfacial fluid into the upper layer. As such, the instabilities and mixing in the stratified shear layer controlled the transport of mass from the bottom to the top layer and hence the deepening of the upper turbulent layer (boundary entrainment).

For the general flow configuration shown in Fig. 1a, SF01 identified the governing parameters, the bulk Richardson number $\mathrm{Ri}_B = \Delta bD/\Delta U^2$ and the frequency ratio $f_N = ND/\Delta U$. They also noted that for the $N = 0$ case the turbulent kinetic energy budget in a control volume delimited by the shear layer thickness δ_s is locally balanced within the error margins of the experiment ($\pm 15\%$), and hence the energetics of mixing within this region ought to be governed by the local parameters such as δ_s and the velocity jump across it ΔU, δ_b and its associated buoyancy jump Δb as well as some nondimensional function Π that takes care of the shapes of the density and velocity profiles. Nonetheless, as far as the overall flow configuration is concerned, all of these parameters are determined by Ri_B, as $f_N = 0$ for this case. When $f_N \neq 0$, the energetics of the shear layer is strongly influenced by the internal wave radiation into the lower layer (especially when $3 < \mathrm{Ri}_B < 5$ or $0.36 < \overline{\mathrm{Ri}}_g < 1$), and hence such a local balance is not possible.

Given the local nature of the energy balance, one may argue that the results obtained for the $f_N = 0$ (two-layer) case can be useful in interpreting other stratified natural shear layers having similar properties. In fact, one of the assumptions made in oceanic microstructure studies is the balance between the local production P, dissipation ϵ, and buoyancy flux B, and hence the mea-

Corresponding author address: Dr. H. J. S. Fernando, College of Engineering and Applied Sciences, Environmental Fluid Dynamics Program, Arizona State University, Tempe, AZ 85287-9809.
E-mail: j.fernando@asu.edu

a.

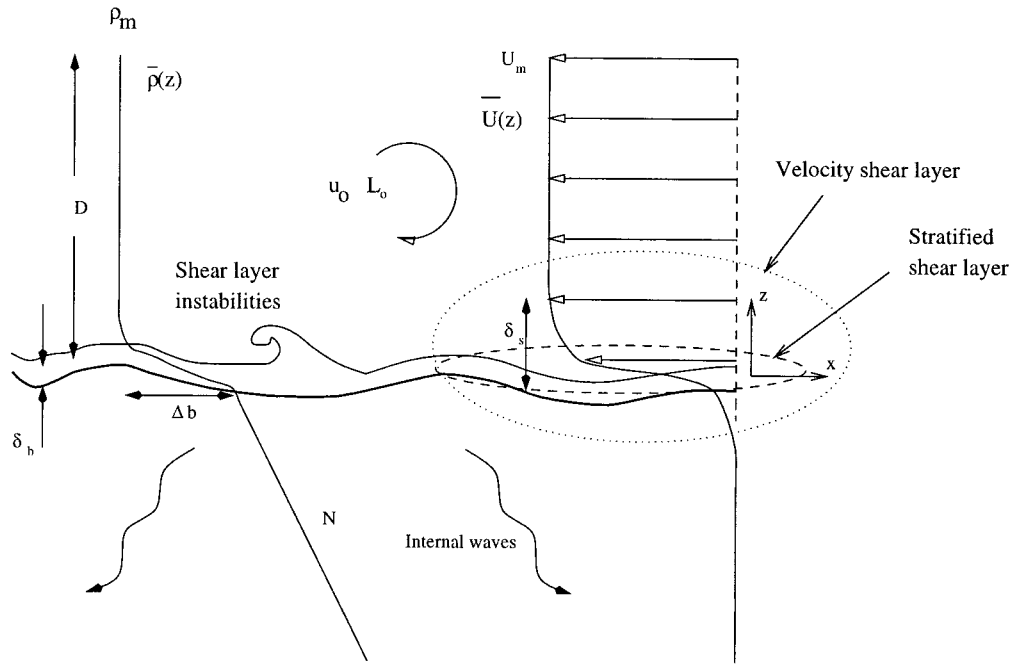

b.

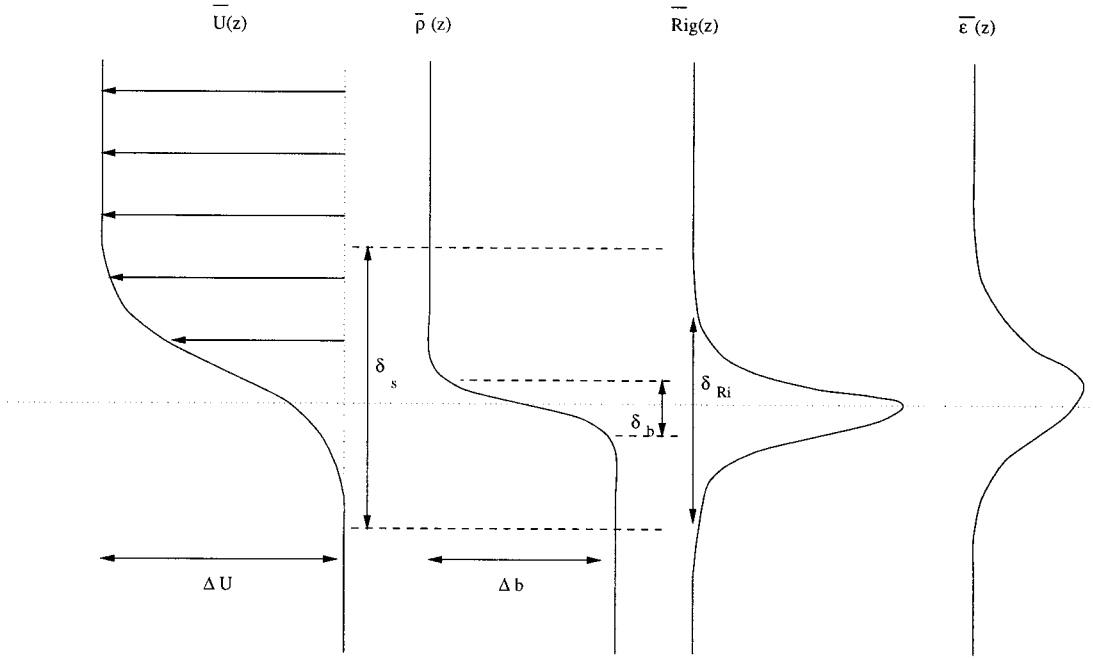

FIG. 1. (a) Schematic of velocity and density fields in the stratified shear layer studied by SF01, and (b) typical $\overline{U}(z)$, $\overline{\rho}(z)$, $\overline{\mathrm{Ri}}_g(z)$, and $\overline{\epsilon}(z)$ distributions in a laboratory shear layer with $f_N = 0$.

surements of SF01 are expected to shed light on these studies. Based on the governing variables identified above, the stratified shear layers in point are expected to be governed by the shear-layer Richardson number $\mathrm{Ri}_s = \Delta b \delta_s / \Delta U^2$, δ_s/δ_b and Π, but their sole dependence on Ri_B suggest that Ri_B should be the sole governing variable. More so, since the (commonly employed) gradient Richardson number Ri_g of the stratified layer is also governed by Ri_B, one may argue that some characteristic Ri_g should adequately describe the nature of the shear layer. Since instantaneous Ri_g is a highly fluctuating quantity, a suitably (time) averaged value can be used instead, namely,

$$\overline{\mathrm{Ri}}_g = \frac{\overline{N_L^2}}{\overline{(\partial u/\partial z)^2}}, \tag{1.1}$$

where N_L is the local buoyancy frequency (based on measurement resolution) and $\partial u/\partial z$ is the local shear. Figure 1b shows the schematics of the profiles of $\overline{U}(z)$, density $\overline{\rho}(z)$, $\overline{\mathrm{Ri}}_g(z)$, and $\overline{\epsilon}(z)$ through the stratified shear layer, based on the experimental procedure described in section 2. Since the vertically averaged $\overline{\mathrm{Ri}}_g$ approximately coincides with that of the top of the density interface, $\overline{\mathrm{Ri}}_g$ measured in the vicinity of the upper boundary of the density interface could be used as the characteristic value.

In identifying shear instabilities, SF01 used quantitative flow vizualization based on laser-induced fluorescence and structure identification techniques. They found that in the range $0.086 < \overline{\mathrm{Ri}}_g < 0.36$, the vertical mixing was dominated by pure Kelvin–Helmholtz (K–H) instabilities. This regime was followed by a transition regime wherein both K–H and ''asymmetric waves'' were present [see Lawrence et al. (1991) for a discussion on these waves] in the range $0.36 < \overline{\mathrm{Ri}}_g < 1$. When $1 < \overline{\mathrm{Ri}}_g < 1.3$, the interface was dominated by ''asymmetric waves.'' Lastly, for $\overline{\mathrm{Ri}}_g > 1.3$, the main interfacial instability was symmetric Hölmböe waves. The nature of the instability was found to be closely related to the rate of transport, and the buoyancy flux had diminished by more than an order of magnitude at $\overline{\mathrm{Ri}}_g \sim 1$ with the disappearance of K–H waves.

A conspicuous application of laboratory stratified shear layer studies is the sheared thermocline in the ocean (Woods 1968) through which transports of heat, mass, and momentum play an important role in oceanic heat and momentum budgets. This mainly occurs through small-scale turbulent mixing, but the exact mechanisms involving such mixing is yet to be determined (Killworth 1998). Since the ultimate goal of ocean mixing studies is the development of predictive models of ocean circulation wherein, at present, small-scale mixing is parameterized in terms of an eddy diffusivity, the focus of ocean mixing studies has been the development of eddy diffusivity parameterizations. In so doing, the buoyancy flux $B = -\overline{b'w'}$ relative to the turbulent kinetic energy (TKE) production is expressed in terms of the mixing efficiency or flux Richardson number Ri_f, namely,

$$\mathrm{Ri}_f = \frac{-\overline{b'w'}}{-\overline{u'w'}\dfrac{d\overline{u}}{dz}} = \frac{B}{P}, \tag{1.2}$$

where P is the production of TKE in the shear layer with mean vertical shear $S = \overline{du}/dz$ and the dissipation flux coefficient (Moum 1996b)

$$\Gamma = \frac{B}{\epsilon} \simeq \frac{\mathrm{Ri}_f}{1 - \mathrm{Ri}_f}, \tag{1.3}$$

where ϵ is the rate of TKE dissipation. Note that the approximation in (1.3) involves an assumption on the energy budget such that

$$P \simeq B + \epsilon, \tag{1.4}$$

which is approximately satisfied in our experiments, as is evident from the energy budget studies discussed in section 3a. This latter section also compares the oceanic and laboratory Ri_f, Γ, and $\overline{\mathrm{Ri}}_g$ measurements and discusses their implications. Because of the difficulties of direct oceanic measurement of $\overline{b'w'}$, it is evaluated indirectly based on (1.4) and certain other approximations. The efficacy of these approximations are discussed in section 3b in light of laboratory measurements.

Questions related to momentum K_m and mass K_ρ diffusivity,

$$K_m = \frac{-\overline{u'w'}}{d\overline{u}/dz} = \frac{P}{S^2} \quad \text{and} \tag{1.5}$$

$$K_\rho = \frac{-\overline{\rho'w'}}{d\overline{\rho}/dz} = \frac{-\overline{b'w'}}{N_L^2} = \frac{B}{N_L^2}, \tag{1.6}$$

are addressed in section 3c. A large number of parameterizations are available in this context, and hence only a selected few of such parameterizations that have direct oceanic applications will be considered.

The oceanic data that were used in comparisons were taken from various reported studies on oceanic stratified turbulent mixing. Particularly attractive were those taken in the equatorial undercurrent (EUC) on which a substantial amount of studies have been reported as a result of the Tropic Heat Experiments conducted in 1984; for example, see Eriksen (1985), Gregg et al. (1985), Moum and Caldwell (1985), Chereskin et al. (1986), and Moum et al. (1989). Figure 2 shows the structure of the Pacific Equatorial Current System, where equatorial currents flow westward over the eastward EUC. Since the EUC is driven by the thermocline tilt induced by the westward wind stress, the core of the EUC is embedded within the thermocline, creating a stratified shear flow seen in Fig. 2. Note the increased turbulent activity (signified by ϵ) in the low Ri_g region above the highly stratified core. Focusing on the EUC seems particularly appropriate given that the widely used eddy diffusivity parameterizations for ocean gen-

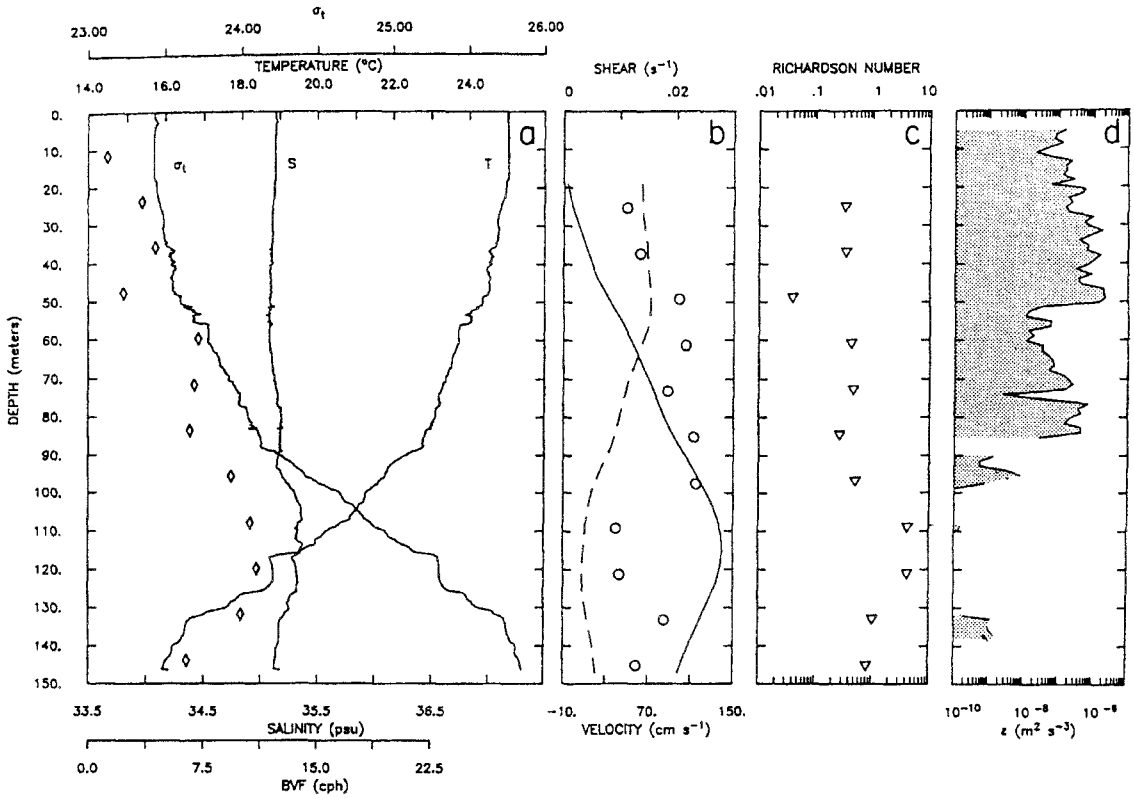

FIG. 2. The depth variations of σ_t, buoyancy frequency, (hourly averaged) shear of the east–west (−) currents, shear magnitude (○), the gradient Richardson number (△), and the dissipation of turbulent kinetic energy (shaded) taken from microstructure measurements at the equator during the Tropic Heat experiment (Moum et al. 1989).

eral circulation models have been tuned for the current and density structure of equatorial undercurrents. Further, the absence of Coriolis forces at the equator prevents complications of velocity vector rotation with depth and hence EUC structure can be discussed in light of laboratory planar stratified shear layers.

Lastly, it should be mentioned that the extrapolation and comparison of laboratory experimental results with ocean measurements (summarized in section 4) should be carried out with caution. In such comparisons, Reynolds number similarity is assumed in the pretext that the laboratory Reynolds numbers (in our case $\mathrm{Re}_s = \Delta U \delta_s / \nu \sim 5000$) are high enough to be in the fully three-dimensional regime (that requires $\mathrm{Re}_s > 1000$) when the flow properties are assumed to be independent of Re_s. Another issue is the measurement resolution Δz_m of Ri_g, wherein Ri_g may depend on Δz_m [for example, see Toole and Schmitt (1987), Polzin (1996), and Kunze et al. (1990)]. Laboratory measurements of Ri_g with varying Δz_m have indicated a strong dependence of Ri_g on Δz_m when Δz_m is larger than the local Ozmidov scale L_o^* (DeSilva et al. 1999). Since $\Delta z_m = 0.25$ cm, $L_o^* \sim$ 0.4–3.2 cm in our experiments, the results presented are expected to be independent of the measurement resolution. Further, the results ought to be able to compare with oceanic measurements taken with $\Delta z_m / L_o^* \leq O(1)$.

Next, the experimental procedure will be described, followed by the energy budget (section 3a), flux parameterizations (section 3b), and eddy diffusivity parameterization (section 3c) studies. Conclusions are given in section 4.

2. Experimental procedure

The experiments were performed in a closed loop water channel facility, similar in design to that of Odell and Kovasznay (1971). Figure 3 presents a schematic of the tank. Through the action of two counterrotating series of disks (separated in the vertical by 1 cm and placed only within the uppermost 15 cm of the fluid column), mean horizontal momentum was imparted to the upper flow. As discussed in Stephenson and Fernando (1991) and SF01, the interaction between the rotating disks and the fluid generates only minimal disturbances and hence minimal turbulence. In the pump section, however, thin plates were placed just below the level of the lowest plates to isolate the pump from the fluid beneath. In addition, as shown in Fig. 3, several flow conditioning devices were used.

The stratification was established using salt and an aqueous solution of ethanol (<10% by volume). Ethanol was introduced to create an optically homogeneous me-

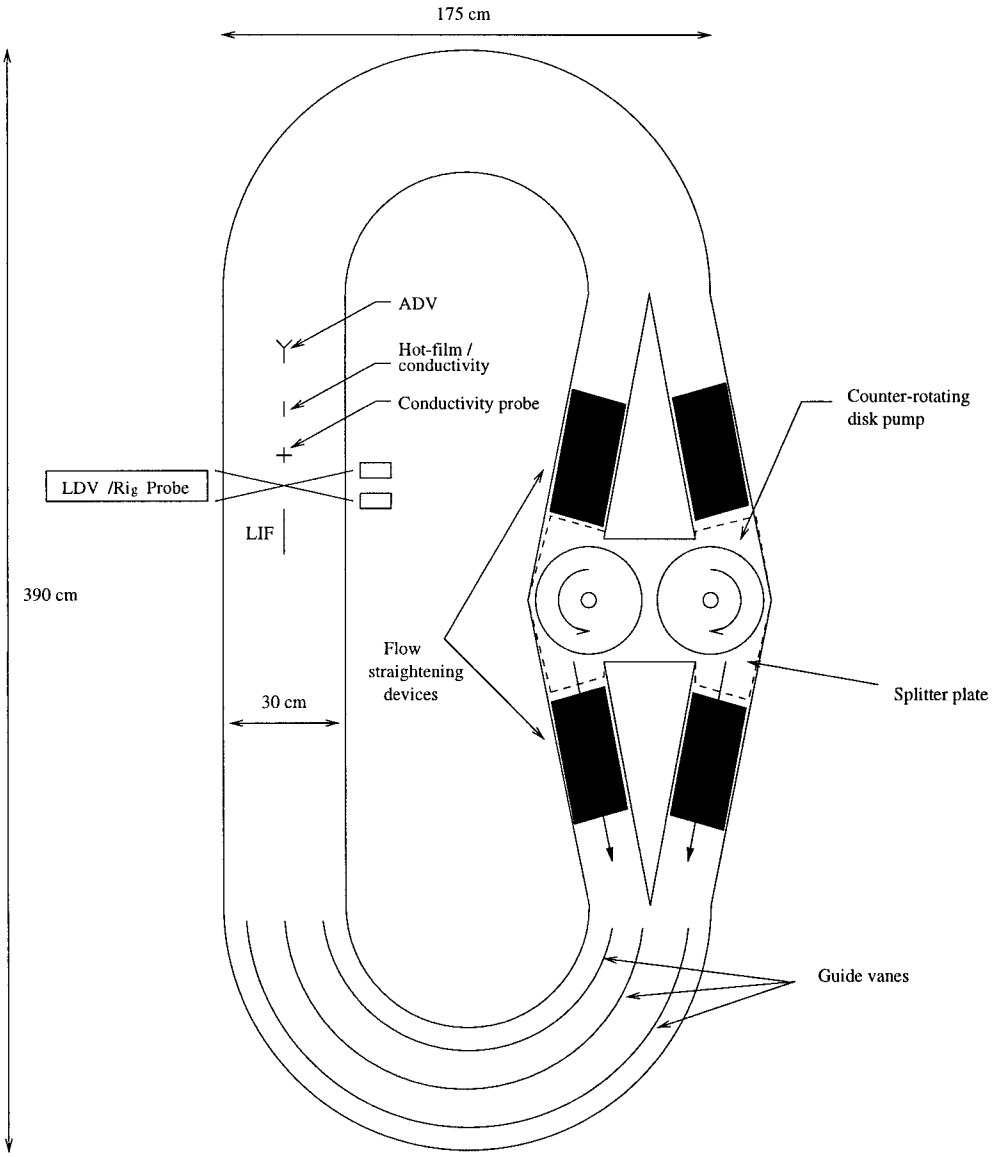

FIG. 3. Schematic of closed-loop Odell–Kovasznay (recirculating) water facility.

dium (through matching the index of refraction between different layers), enabling the use of optical measurement techniques. Because of the difficulties associated with using hotfilm probes in a linearly stratified layer at low velocities, the current experiments were conducted with a two-layer configuration (i.e., $N = 0$). Experimental parameter ranges included $5.0 < \Delta U$ (cm s^{-1}) < 15.0, $15.0 < D$ (cm) < 28.0, and $2.0 < \Delta b$ (cm s^{-2}) < 75.0.

Measurement instruments included a custom-built, two-point, single-component laser Doppler velocimeter (LDV), a laser-induced fluorescence (LIF) system, microscale conductivity probes, an acoustic Doppler velocimeter (ADV), and a two-component X-type hotfilm (see Fig. 3 for the location of these measurement devices). Operational procedures of LDV, ADV, and X-type hotfilm probes are standard, and are not discussed here. The methods for data acquisition and processing are discussed in length in Strang (1997). An in-house-built two-point LDV was juxtaposed with a two-point conductivity probe, thus enabling the measurement of the local gradient Richardson number. The vertical separation of probe volumes for both the LDV and conductivity probes were 2.5 and 2.3 mm, respectively [see DeSilva (1991) and DeSilva et al. (1999)].

Measurements of Ri_g were obtained by locating the local gradient Richardson number probe below the velocity and buoyancy interfacial layers and recording continuous time realizations as the interfacial region descended past the probe. An example of time traces of density so obtained from the two conductivity probes are shown in Fig. 4a. Note that at time $t < 10$ sec (here

t is a measure of the time elapsed since the initiation of the data sample) the probe is submersed within the dense homogeneous fluid below the interface, and by $t = 15$ sec the probe is entirely within the interfacial layer. When $15 < t < 50$ sec, the measurement is considered to be taken in the stratified shear layer. For these times, the respective time traces of the density and velocity gradients and the gradient Richardson number $\mathrm{Ri}_g = -g/\rho_o(\partial\rho/\partial z)/(\partial u/\partial z)^2$ are shown in Figs. 4b, 4c, and 4d based on the instantaneous density ρ and horizontal velocity u. Here g is the gravitational acceleration. Generally, time realizations were taken on 32-s intervals (separated by 10 s) at a sampling frequency of 128 Hz [see Strang (1997) and SF01 for more details regarding the signal processing, including the selection of averaging timescales]. In determining the averaged local gradient Richardson number $\overline{\mathrm{Ri}}_g$ in the stratified shear layer, time averages were employed for the density and velocity gradients individually, and then the definition for $\overline{\mathrm{Ri}}_g = \overline{N_L^2}/\overline{\partial u/\partial z^2}$, where the overbar denotes the respective time average, was used. Averaging should be performed for stationary time traces, and averaging times were selected after careful consideration of the time traces. The timescale τ selected for averaging was sufficiently long to resolve integral scales; however, it was substantially short (<5%) when compared to the interfacial deepening timescale (i.e., $\tau_L \ll \tau < 0.05D(dD/dt)^{-1}$). Therefore, when $\overline{\mathrm{Ri}}_g < 1$, the averaging timescale was generally some fraction of the sampling period. The procedure adopted to obtain stable mean averages in the presence of a long-time scale nonstationarity is described in SF01. A profile of $\overline{\mathrm{Ri}}_g$ so obtained was shown in Fig. 1b.

Rhodamine 6G–based laser-induced fluorescence technique [for details, see De Silva et al. (1990, 1996) and Strang (1997)] was employed to perform detailed flow visualization of interfacial instability and to obtain quantitative information on a two-dimensional swath through the test section. Time-evolving LIF images taken through this plane, which was illuminated by an Argon ion laser sheet emanating from a scanner, were recorded onto a magnetic medium using a SVHS recorder. The approximate spatial resolution (in the streamwise and vertical directions) of the measurement was 0.16 mm, and the frequency resolution was 60 Hz. In light of the thickness of the laser sheet (~0.9 mm) and the restricted frequency and spatial resolution of the charge coupled device (CCD) camera, this approach does not resolve the smallest (Batchelor) scales of buoyancy fluctuations. However, in addition to quantitative flow visualization, LIF provides sufficient resolution for the integral properties measured, that is, buoyancy flux.

The dissipation of turbulent kinetic energy ϵ was evaluated by using the hotfilm anemometry records and the assumptions of local isotropy [$\epsilon = 7.5\nu\overline{(\partial u/\partial x)^2}$, where $\partial u/\partial x$ is the instantaneous streamwise velocity gradient] and frozen turbulence hypothesis. Although the local isotropy assumption is questionable for this highly stratified shear layer, it has been shown that small scales of stratified turbulence can still be treated as isotropic when $(\epsilon/\nu N^2)^{3/4} \gg 200$ (Gargett et al. 1984), and this condition is approximately satisfied locally in our measurements when $z/\Delta_b > 1$ [also see Itsweire et al. (1993) for a comprehensive discussion on the evaluation of ϵ]. Under these conditions, the anisotropy of turbulence is primarily confined within the interfacial buoyancy layer $|z/\delta_b| < 1$ such that the layer-averaged TKE dissipation rate $\langle\epsilon\rangle$ is not dramatically affected. As will be discussed later, both the shear and buoyancy production of turbulence were computed directly from measurements of the Reynolds stress component ($\overline{u'w'}$) and the turbulent buoyancy flux ($\overline{b'w'}$) using the two-component X-type hotfilm placed in close proximity with a microscale conductivity probe (separation distance less than 1 mm). The vertical shear ($\partial\overline{u}/\partial z$) was estimated via fitting the vertical profile of mean streamwise velocity with a hyperbolic tangent function (Strang 1997; SF01). The systematic calibration errors for the hotfilm measurements were ±0.5%, and the total cumulative errors of measurements were estimated as ±15% for ϵ, ±18% for P, and ±5% for B.

Based on the time averaging procedure presented above, multiple samples were acquired across the stratified shear layer to obtain vertical profiles of averaged quantities, such as mean velocities and density, respective variances, shear and buoyancy production of turbulence, and the rate of TKE dissipation. In addition to time averaging, vertical averaging across the stratified shear layer was utilized for estimating such properties as the shear production P, the buoyancy flux B, and the TKE rate of dissipation ϵ. These vertically averaged quantities are hereinafter represented with angular brackets, for example, $\langle\epsilon\rangle = (\int_0^D \epsilon\, dz)/D$, where the lower bound of the integration represents the interface center; however, see section 3 for the exact upper limit used in the integration. Using the above vertically integrated quatities, the characteristic parameters that represent mixing, such as Ri_f, Γ, and K_ρ and K_m, were estimated, and they will be denoted with the overbar, that is, $\overline{\mathrm{Ri}}_f$, $\overline{\Gamma}$, $\overline{K}_m$, and $\overline{K}_\rho$.

3. Experimental results

a. Mixing efficiency and dissipation flux coefficient

The energetics of the stratified shear layer was evaluated by using two methods, point-by-point local measurements and layer-averaged quantities. In the former method, ϵ, B and P were measured across the shear layer along a vertical line to evaluate the terms of the horizontally homogeneous form of the turbulent kinetic energy equation, namely,

$$\frac{\partial(\overline{q^2/2})}{\partial t} = P - B - \frac{\partial}{\partial z}\left[\overline{w'\left(\frac{p'}{\rho_o} + \frac{q^2}{2}\right)}\right] - \epsilon. \quad (3.1)$$

Equation (3.1), when integrated across the mixed layer, takes the form

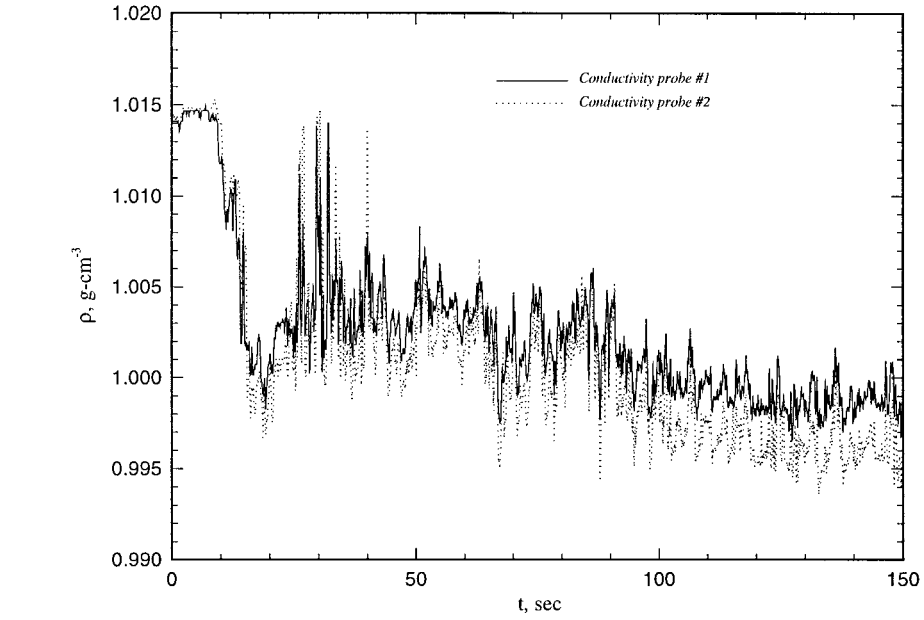

a.

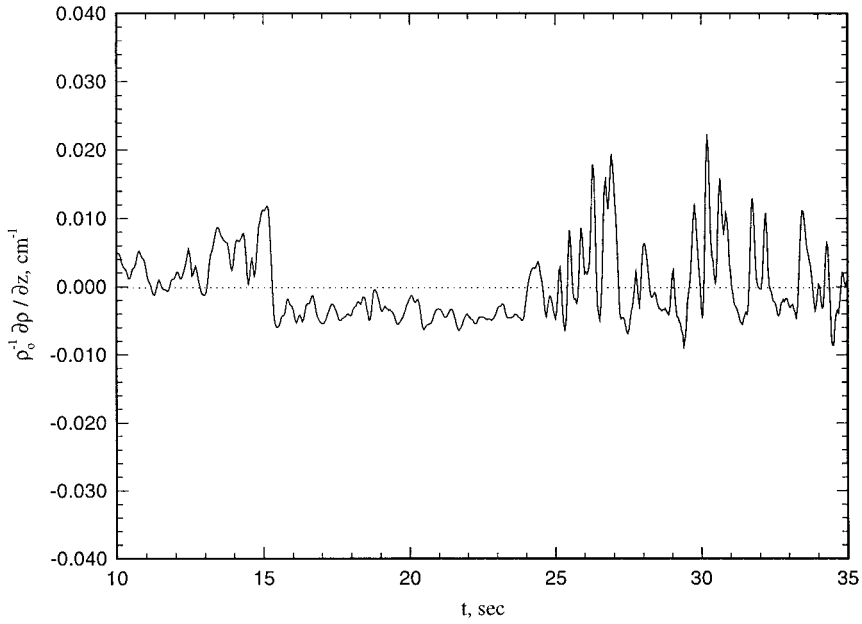

b.

FIG. 4. (a) Time trace of density across density interface and mixed layer base (two-point probe), $0.28 < \overline{\mathrm{Ri}}_g < 0.41$; (b) time trace of vertical gradient of density, $\rho_o^{-1}\partial\rho/\partial z$, at the mixed layer base; (c) time trace of vertical gradient of velocity, $\partial u/\partial z$, at the mixed layer base; (d) time trace of the gradient Richardson number, Ri_g. The enlarged region of (b) and (c) are also indicated.

$$\int_0^D \frac{\partial \overline{q^2/2}}{\partial t} = \int_0^D P\, dz - \int_0^D B\, dz - \int_0^D \epsilon\, dz + \overline{w'\left(\frac{p'}{\rho_o} + \frac{q^2}{2}\right)}\Bigg|_{z=0}, \tag{3.2}$$

where the divergence term vanishes in the upper limit ($z = D$). Because of the possible energy leakage to the motion field in the bottom layer, the energy flux through the middle of the interface (in an average sense) located at $z = 0$ is generally nonzero. Careful evaluation of data, however, indicated that the upper limit of the in-

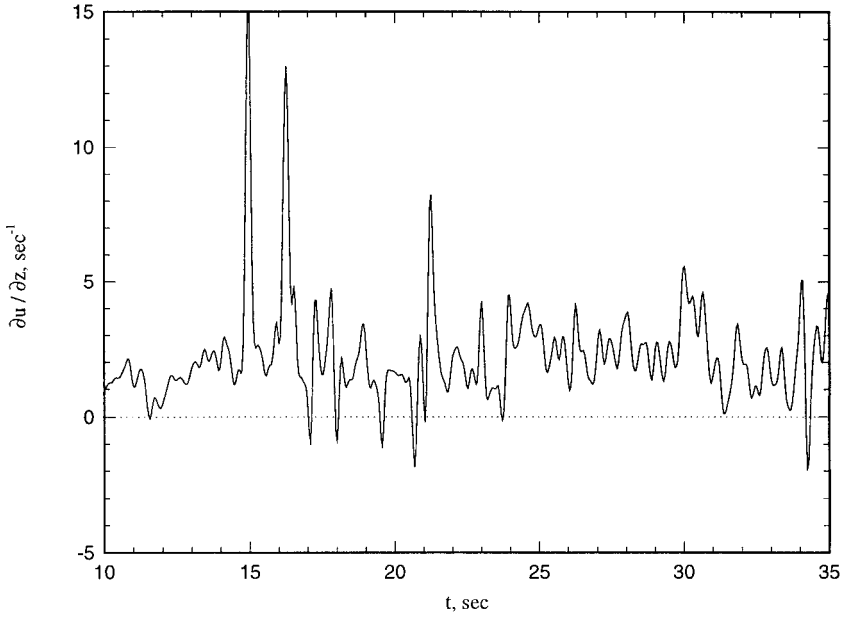

c.

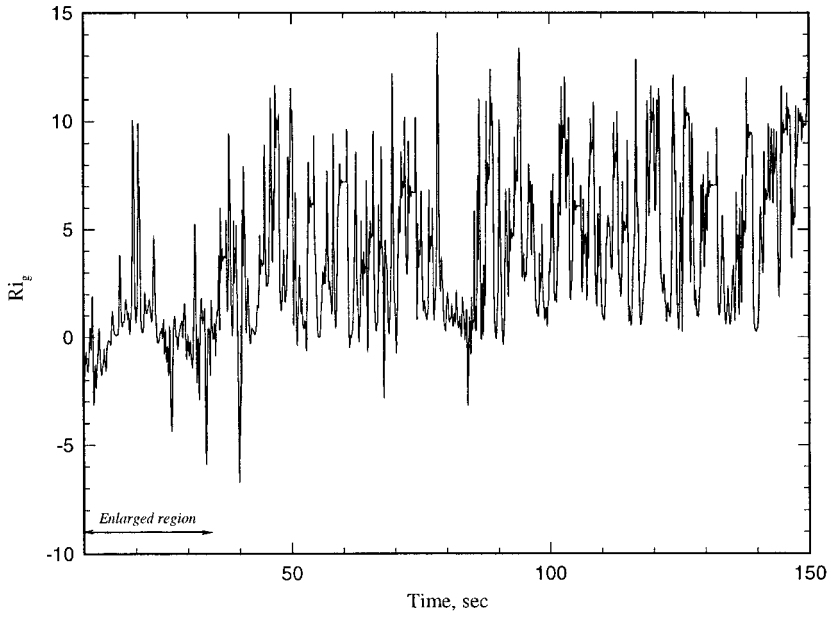

d.

FIG. 4. (*Continued*)

tegration can be much less than $z = D$, of the order of 1.5 times the shear layer thicknesses ($z \sim 1.5\delta_s$), because there is only an insignificant amount of energy flux passing through that level. Thus, the location where P falls to 5% of its maximum was selected as the upper limit of integration. For the two-layer case investigated, the energy flux crossing $z = 0$ is expected to be negligible, given the weak motions detected in the lower layer.

The vertical spatial averages of P, B, and ϵ, $\langle P \rangle$, $\langle B \rangle$,

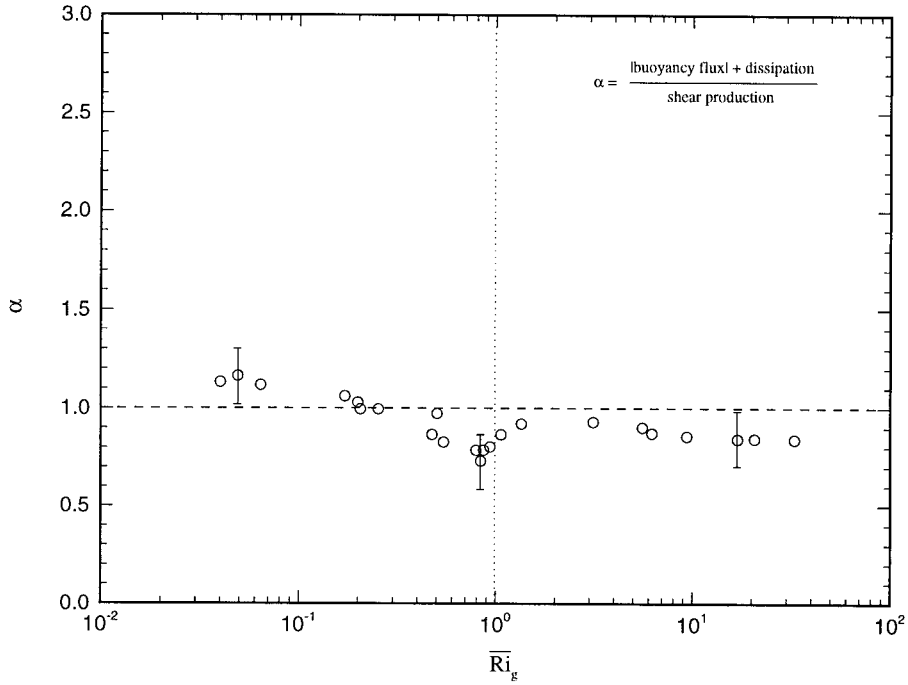

FIG. 5. Variation of TKE budget parameter α with $\overline{\mathrm{Ri}}_g$.

and $\langle \epsilon \rangle$ (in the depth range of integration) could be used to evaluate the quasistationarity of the stratified shear layer and, thereby, substantiate the extent to which there exists a balance between the shear production of turbulence and the sum of the turbulent buoyancy flux and TKE dissipation rate, namely,

$$\langle P \rangle \simeq \langle B \rangle + \langle \epsilon \rangle \tag{3.3}$$

A useful measure in this context is

$$\alpha = (\langle B \rangle + \langle \epsilon \rangle)/\langle P \rangle, \tag{3.4}$$

which is unity according to (3.3) when the flow is stationary and the flux divergence is zero at either limit of the integration. The plot of α versus $\overline{\mathrm{Ri}}_g$, shown in Fig. 5, indicates that (3.3) is approximately satisfied except at around $\overline{\mathrm{Ri}}_g \sim 0.25 - 1$ where the interfacial activity is pronounced. The value of α at large $\overline{\mathrm{Ri}}_g$ is somewhat smaller than 1.0, but the error bars around most of the data points encompass $\alpha = 1$. On the other hand, $\alpha < 1$ may indicate some energy leakage into the base of the bottom layer to excite motions there [when $\overline{\mathrm{Ri}}_g > 1$, the flow is quasistationary, and the first term in (3.1) is negligibly small]. At smaller $\overline{\mathrm{Ri}}_g$, α tends to increase above unity, indicating the influence of the time-dependent term in (3.1).

The data presented in Fig. 5 allow the calculation of the layer-averaged form of the flux Richardson number,

$$\overline{\mathrm{Ri}}_f = \frac{\langle B \rangle}{\langle P \rangle}, \tag{3.5}$$

or the dissipation flux coefficient,

$$\overline{\Gamma}_o = \frac{\langle B \rangle}{\langle \epsilon \rangle}. \tag{3.6}$$

Figure 6 shows the dependence of $\overline{\Gamma}_o$ and $\overline{\mathrm{Ri}}_f$ on $\overline{\mathrm{Ri}}_g$. Note that the mixing efficiency drastically increases in the range $0.15 < \overline{\mathrm{Ri}}_g < 1$, with the peak efficiency of $\overline{\mathrm{Ri}}_f \simeq 0.4$ occurring at $\overline{\mathrm{Ri}}_g \simeq 1$. It is within this $\overline{\mathrm{Ri}}_g$ range that K–H instabilities and asymmetric waves in the stratified shear layer coexist and perhaps resonate with each other, as pointed out by SF01. The results of SF01 also showed that at $\overline{\mathrm{Ri}}_g \sim 1$, the production rate of density flux at the interface is in balance with the rate at which the density flux is carried away by the turbulent eddies in the contiguous turbulent layer (i.e., there is no accumulation of partially mixed fluid at the interface). The dissipation flux coefficient $\overline{\Gamma}_o$ shown in Fig. 6 varies between 0.06 and 0.65, which is in reasonable agreement with the oceanic measurements of Moum et al. (1989), who reported $0.12 < \Gamma_o < 0.48$.

The present data can be compared with those compiled by Ivey and Imberger (1991) based on laboratory experiments with and without shear. They rescaled stratified turbulence data using two governing parameters, the overturning Froude number $\mathrm{Fr}_T = u/NL$ and the Reynolds number $\mathrm{Re}_T = uL/\nu$, where u and L are the rms velocity and energy containing eddy size of turbulence. Given that $\mathrm{Ri}_g = N^2/(\Delta U/\delta_s)^2 \sim N^2L^2/u^2$, their Fr_T is expected to be related to $\overline{\mathrm{Ri}}_g$,used herein as $\overline{\mathrm{Ri}}_g \propto \mathrm{Fr}_T^{-2}$. Ivey and Imberger (1991) noted that the maximum flux Richardson number Ri_f ($\sim$0.2) occurs at $\mathrm{Fr}_T \sim 1$, bounded by decaying values of Ri_f for increasing

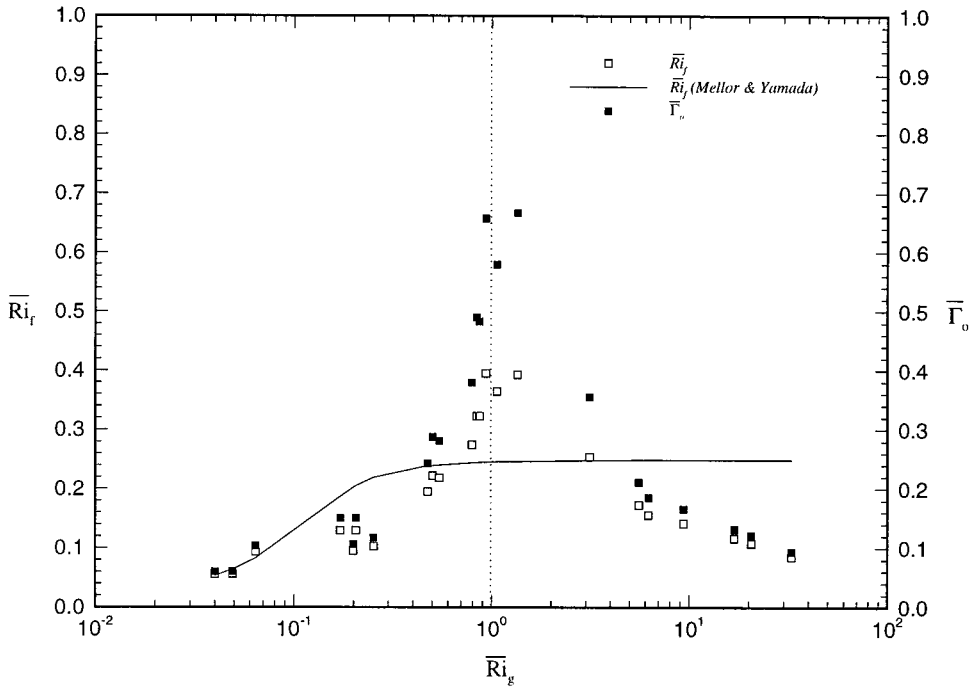

FIG. 6. Variation of flux Richardson number $\overline{\mathrm{Ri}}_f$ (open squares) and dissipation flux coefficient $\overline{\Gamma}_o$ (solid squares) with $\overline{\mathrm{Ri}}_g$.

and decreasing Fr_T. Our observation of the maximum Ri_f occurring at $\overline{\mathrm{Ri}}_g \sim 1$ is consistent with their observations, although the maximum in the present case is a factor of 2 higher. Ivey and Imberger (1991) also noted that the maximum Ri_f is sensitive to the Prandtl number and the Reynolds number of the flow. With regard to the latter, Ri_f was argued to be increasing with Re_T until a maximum is reached. Their data covered the range $6 \leq \mathrm{Re}_T \leq 17$, wherein for $\mathrm{Fr}_T \sim 1$ at $\mathrm{Re}_T \sim 17$, Ri_f is approximately 0.2. It is not clear whether the increase of Re_T beyond this Re_T will give rise to at least a slow increase of the maximum Ri_f. Therefore, our measurements of the maximum Ri_f made in the range $15 < \mathrm{Re}_T < 100$ may not be directly compared quantitatively with those reported by Ivey and Imberger (1991).

Mellor and Yamada (1974) developed a hierarchy of turbulence models with varying complexity for geophysical turbulence. The most complex model employed ten partial differential equations in addition to the mean velocity components and temperature, whereas the least complex eliminated all ten equations. The level 2 and 2.5 (Mellor and Yamada 1982) models were the most attractive, in which the momentum and heat transports were written in gradient transport form with eddy coefficients that depend on $\Gamma = \mathrm{Ri}_f/(1 - \mathrm{Ri}_f)$. The level 2 model, based upon empirically determined constants, postulates a relation between Ri_f and $\overline{\mathrm{Ri}}_g$, namely,

$$\mathrm{Ri}_f = 0.725(\overline{\mathrm{Ri}}_g + 0.186 - (\overline{\mathrm{Ri}}_g^{\,2} - 0.316\overline{\mathrm{Ri}}_g + 0.0346)^{1/2}), \quad (3.7)$$

plotted in Fig. 6. The level 2 model (solid line) predicts $\overline{\mathrm{Ri}}_f$ to rise from approximately 0.05 (at $\overline{\mathrm{Ri}}_f \sim 0.04$) to a value of 0.245 at $\overline{\mathrm{Ri}}_g = 1$. It is at $\overline{\mathrm{Ri}}_g \sim 1$ that $\overline{\mathrm{Ri}}_f$ has reached 99% its maximum value. Beyond $\overline{\mathrm{Ri}}_g \sim 1$, $\overline{\mathrm{Ri}}_f$ appears to be independent of $\overline{\mathrm{Ri}}_g$. In general, the level 2 model of Mellor and Yamada (1974) does not agree with our data except that $\overline{\mathrm{Ri}}_f$ reaches a maximum beyond $\overline{\mathrm{Ri}}_g \sim 1$.

The observation of maximum mixing efficiency at $\overline{\mathrm{Ri}}_g \sim 1$, whence the K–H instabilities coexist with asymmetric waves in the stratified shear layer, can be compared with observations made in deep and coastal oceans. At the outset, it should be noted that the Miles–Howard linear stability analysis, which predicts the possibility of shear instabilities and turbulence in stratified shear layers when $\mathrm{Ri}_g < ¼$, is commonly used for interpretation of oceanic observations. Given the intense background forcing, turbulence, and nonstationarity of the thermocline motions, it is, however, not clear whether the linear stability predictions above are directly applicable to oceanic stratified layers. For example, stability analyses of Majda and Shefter (1998) clearly show that the nonstationarity of the flow drastically alters stability characteristics. More so, comparison of oceanic data with theory has to be done with care, as most oceanic Ri_g data are averaged over considerable time periods. As such, energy-based stability estimates such as those described by Richardson (1920) and Miles (1986) are more appropriate for oceanic conditions. These estimates predict $\mathrm{Ri}_g > 1$ as the condition for the

decay of disturbances in stratified shear layers. The Liapunov stability analysis of Arbabanel et al. (1986) also shows a critical Richardson number of unity.

A number of $\overline{\mathrm{Ri}}_g$ measurements based on moored and ship-based observations have been reported in the past several decades. An example is the Tropic Heat Experiment in the equatorial Pacific, which showed a consistent pattern of intense mixing in the low $\overline{\mathrm{Ri}}_g$ zone above the velocity maximum of the undercurrent core, weak mixing in the undercurrent core, and moderate to intense mixing in the low $\overline{\mathrm{Ri}}_g$ zone below the core (Gregg 1976; Moum et al. 1989). Moum et al. (1989) reported that in the highly sheared zone of the EUC (at depths < 90 m), $\overline{\mathrm{Ri}}_g$ (based on 12-m resolution) varied in the range 0.15 to 1.0, and in the moderately sheared and highly stratified region below the velocity maximum $\overline{\mathrm{Ri}}_g$ remained approximately unity. Peters et al. (1988) also found the shear zone above the undercurrent core to have $1/4 < \overline{\mathrm{Ri}}_g < ½$. Chereskin et al. (1986) and Toole et al. (1987) reported that $\overline{\mathrm{Ri}}_g$ (measured with resolutions of 12 and <3 m, respectively) above the EUC has values less than 0.25 in the upper 50 m surface mixed layer. These observations suggest that the highly sheared and stratified zones in the EUC are at or around the maximum mixing efficiency (Ri_f) limits, and K–H instabilities should be a prevalent feature above and below the EUC core. This conjecture is consistent with K–H signatures reported by Hebert et al. (1992) and De Silva et al. (1996) in EUC.

In the main thermocline near Bermuda, Eriksen (1978) found that $\overline{\mathrm{Ri}}_g$ (resolution of 7 m) varied between 0.25 and 1 during certain overturning events (which were identified as breaking internal waves caused by K–H instability due to internal shear of such waves), but for stable conditions $\overline{\mathrm{Ri}}_g > 1$. The observations of Halpern (1976) carried out off the coast of Oregon during the upwelling season showed that $\overline{\mathrm{Ri}}_g$ is generally high (10–100) except during the upwelling events where it dropped below unity, whence vertical mixing of temperature occurred. Kundu and Beardsley (1991) obtained $\overline{\mathrm{Ri}}_g$ data off the northern California coast during the upwelling season; their data mostly lie in the range $0.15 < \overline{\mathrm{Ri}}_g < 1$, except under highly stable conditions where $\overline{\mathrm{Ri}}_g > 1$.

In summary, $\overline{\mathrm{Ri}}_g$ data for oceanic stratified shear layers generally tend to fall into a regime where the mixing efficiency is at or around the peak values. When the stratification is strong, $\overline{\mathrm{Ri}}_g$ is expected to sporadically drop below unity, thus causing intermittent mixing due to K–H billowing. These regions are characterized by high local shear and contributed by internal waves, background mean shear, and turbulence. According to Thompson (1984), the analysis of oceanic Ri_g data of DeSaubies and Smith (1982) indicates that the probability of shear-controlled mixing in oceans becomes negligible when $\overline{\mathrm{Ri}}_g > 1.33$. This observation is not far out from the data presented in Fig. 6.

b. Evaluation of oceanic flux parameterizations

The present measurements can be used to evaluate the efficacy of methodologies that are being used to calculate oceanic fluxes. Because of the motion fields associated with measuring vehicles and the difficulty of eliminating internal-wave contributions to the measured fluxes, oceanic studies employ indirect methods of estimating buoyancy fluxes using either $\overline{\epsilon}$ or the temperature dissipation rate $\overline{\chi}$, both of which can be evaluated using microstructure data with reasonable accuracy. For example, by assuming stationarity of oceanic flows, Osborn (1980) estimated the volume-averaged diffusivity based upon (3.3). Using $\overline{\mathrm{Ri}}_f$ in (3.5) and $\overline{\Gamma}_o$ from (3.6), (3.3) was reorganized as

$$\langle B\rangle = \overline{\Gamma}_o\langle\epsilon\rangle \simeq \frac{\overline{\mathrm{Ri}}_f\langle\epsilon\rangle}{1 - \overline{\mathrm{Ri}}_f}. \tag{3.8}$$

Osborn (1980) assumed an upper bound for $\overline{\mathrm{Ri}}_f \simeq 0.15$, yielding $\overline{\Gamma}_{o\max} \simeq 0.2$ and $K_\rho \leq 0.2\ \langle\epsilon\rangle/\langle N^2\rangle$ [Osborn (1980) notes that their measurements of dissipation as well as other mean flow measurements represent an integrated version of the TKE equation]. This estimate was consistent with microstructure observations within turbulent patches in the main thermocline (Moum 1996a) that showed $0.15 < \overline{\Gamma}_o < 0.2$. The present results (Fig. 6), however, show that the maximum $\overline{\mathrm{Ri}}_f$ is approximately 0.4 or $\overline{\Gamma}_{o\max} \sim 0.66$, indicating that the maximum $\overline{\mathrm{Ri}}_f$ limit of Osborn should be revisited, with the new limit being $K_\rho < 0.66\ \langle\epsilon\rangle/\langle N^2\rangle$. This new limit is supported by the measurements of Gargett and Moum (1995), who found $\overline{\Gamma}_o$ values as high as 0.7 within turbulent tidal fronts.

Figure 7 shows a plot of (estimated) $K_\rho = \overline{\Gamma}_o\ \langle\epsilon\rangle/\langle N^2\rangle$ versus direct measurements of $K_\rho = \langle B\rangle/\langle N^2\rangle$ via $\overline{b'w'}$ measurements. The dashed line represents the perfect correlation between the estimation and measurements. The open circles indicate the calculations based upon $\overline{\Gamma}_o = 0.2$, and the solid squares indicate the estimation based on $\overline{\Gamma}_o = \overline{\mathrm{Ri}}_f/(1 - \overline{\mathrm{Ri}}_f)$, where $\overline{\mathrm{Ri}}_f = \overline{\mathrm{Ri}}_f(\overline{\mathrm{Ri}}_g)$ is evaluated using Fig. 6. The data clearly indicate that the estimates based upon a constant $\overline{\Gamma}_o$ are unsatisfactory in predicting fluxes (the deviation from the direct measurement can range from 30% to 150%), and the use of $\overline{\mathrm{Ri}}_g$-dependent mixing efficiency can give useful estimates for buoyancy fluxes in stratified shear layers (the deviation from the direct measurement can range up to 30%). This underscores the importance of the measurement of a Richardson number, in addition to $\langle\epsilon\rangle$, when the flux calculations are to be performed using (3.8).

Another method, due to Osborn and Cox (1972), is based on the measurement of the dissipation rate of mean-square temperature fluctuations $\overline{\chi}_T$; this method is sometimes referred to as the dissipation method (Gargett and Moum 1995). Under the steady-state assumption, $\overline{\chi}$ should balance the rate of production of tem-

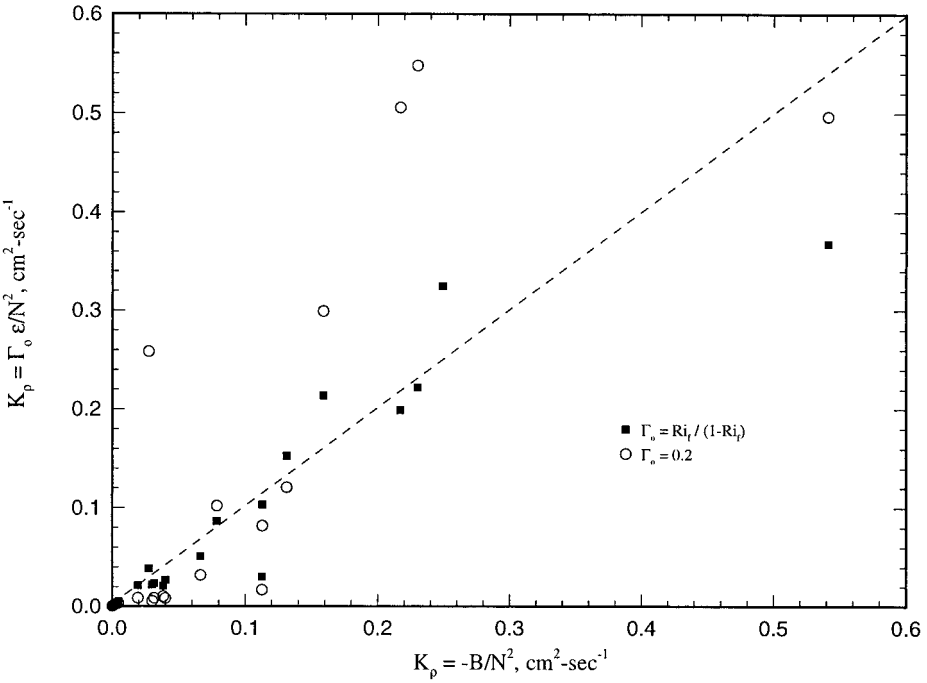

FIG. 7. Comparison of eddy diffusivity for density; K_ρ estimated using (i) $\Gamma_o = \mathrm{Ri}_f/(1 - \mathrm{Ri}_f)$ (solid squares), and (ii) $\Gamma_o = 0.2$ (open circles), vs K_ρ determined directly from $K_\rho = B/N^2$.

perature fluctuations $-\overline{w'T'}\ \overline{dT}/dz$, and hence the temperature diffusivity K_T can be written as

$$K_T = \frac{0.5\overline{\chi}_T}{(d\overline{T}/dz)^2}. \tag{3.9}$$

With the further assumption that heat and salt in the oceans are mixed with equal rates $K_T \simeq K_\rho$, (3.9) can be used to evaluate the buoyancy flux

$$-\overline{b'w'} = \frac{0.5\overline{\chi}}{(d\overline{T}/dz)^2}\frac{d\overline{b}}{dz} = -\overline{b'w'}_d, \tag{3.10}$$

where $\overline{b'w'}_d$ represents the flux calculations based on temperature dissipation measurements. Ideally, one may expect from (3.8) and (3.10)

$$\overline{\Gamma}_o \simeq \overline{\Gamma}_F = \frac{0.5\langle\chi_T\rangle\langle N^2\rangle}{(\langle d\overline{T}/dz\rangle)^2\langle\epsilon\rangle}, \tag{3.11}$$

if all assumptions made in the derivations of (3.8) and (3.10) are satisfied. Here $\overline{\Gamma}_F$ denotes the estimated value of $\overline{\Gamma}_o$ by the dissipation method described above. In the present experiments, the flux dissipation coefficient $\overline{\Gamma}_F$ of (3.11) was obtained using density fluctuations associated with salinity fluctuations (rather than the temperature field). The rate of dissipation of mean-square salinity fluctuations $\overline{\chi}_S$ was ascertained from scalar wavenumber (k) spectra wherein the spectrum takes the form,

$$E(k) = 0.5\overline{\chi}_S\epsilon^{-1/3}k^{-5/3}, \tag{3.12}$$

in the inertial subrange (Oboukhov 1949; Corrsin 1951). Figure 8 presents a representative set of scalar spectra for different locations across the stratified shear layer (each spectrum is taken at a location z normalized by the density layer thickness δ_b where $z = 0$ is the center of the stratified interface). The data exhibit an inertial subrange, in particular, farther from the center of the stratified shear layer where turbulence tends to behave in a more isotropic manner; that is, $z/\delta_b \geq 1$. Near the interface, the inertial subrange exhibits closer to a k^{-2} spectrum, and hence fitting errors are expected. Figure 9 presents the dependence of the layer-averaged flux dissipation coefficient $\overline{\Gamma}_F$ on the gradient Richardson number (open squares). The solid squares indicate estimations of $\overline{\Gamma}_o$ from the flux Richardson number measurements [see (3.8)]. For all $\overline{\mathrm{Ri}}_g$, $\overline{\Gamma}_F$ underestimates $\overline{\Gamma}_o$ evaluated using (3.8). The flux dissipation coefficient is underpredicted by a factor of 1.6–4.2, as shown in Fig. 10, where the ratio of the two predictions are simply replotted with the gradient Richardson number.

The existing oceanic datasets suggest that $0.1 < \overline{\Gamma}_F < 0.4$. This agrees well with the present experiments that indicate $0.01 < \overline{\Gamma}_F < 0.38$. In the data of Gargett and Moum (1995) for turbulent tidal flows, the ratio $\overline{\Gamma}_o/\overline{\Gamma}_F$ was found to be in the range of 1.9–4.4; this also is in good agreement with the present measurements. It should be noted that the consistent underprediction of $\overline{\Gamma}_o$ using the dissipation method may be due to the absence of a well-defined $k^{-5/3}$ behavior in the scalar spectra in the strongly stratified region of the shear layer, as stated above. Only the measurements taken at $z/\delta_b > 1$ showed a well-defined $k^{-5/3}$ slope. It is expected that

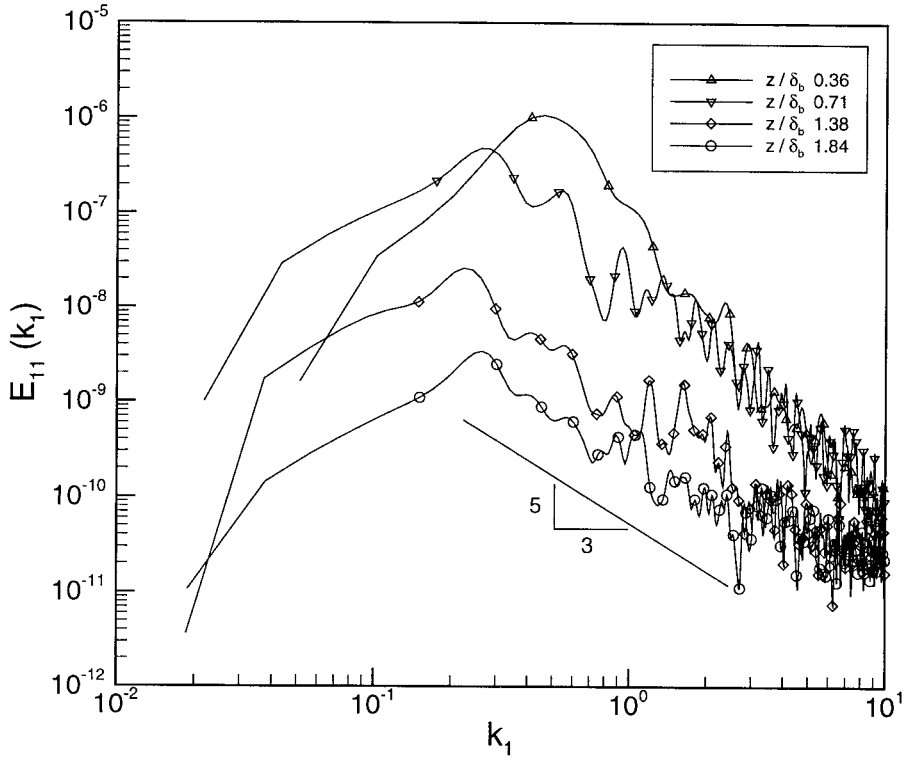

FIG. 8. Scalar wavenumber spectrum presented as a function of the normalized distance from the interface center, i.e., $z/\delta_b = 0$ is the center of the density interface.

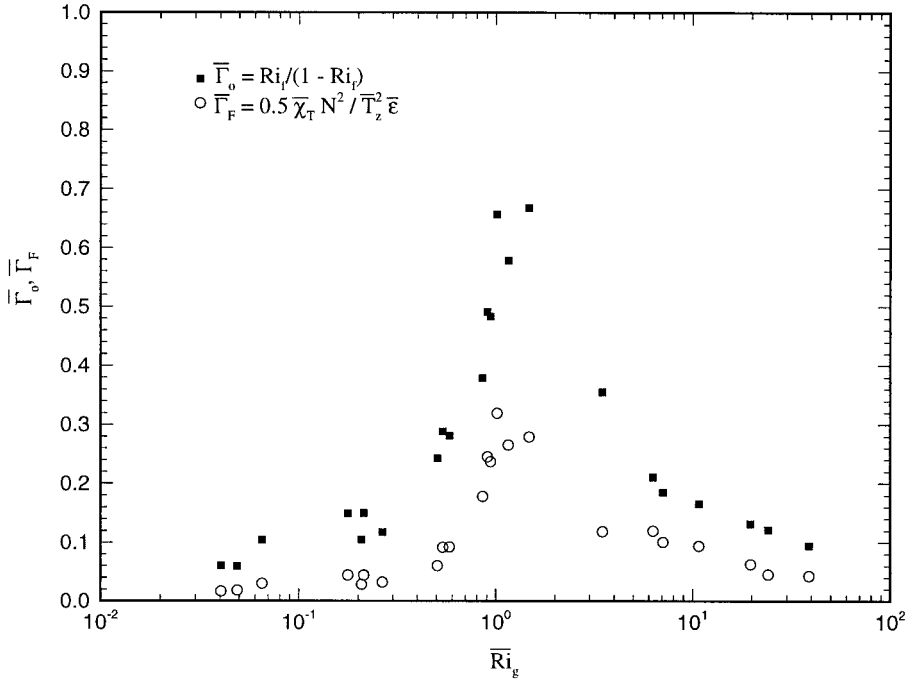

FIG. 9. Comparison of dissipation flux coefficient: (i) $\overline{\Gamma}_o = \mathrm{Ri}_f/(1 - \mathrm{Ri}_f)$ and (ii) $\overline{\Gamma}_F = 0.5\overline{\chi}_T N^2/\overline{T}_z^2\overline{\epsilon}$ vs $\overline{\mathrm{Ri}}_g$.

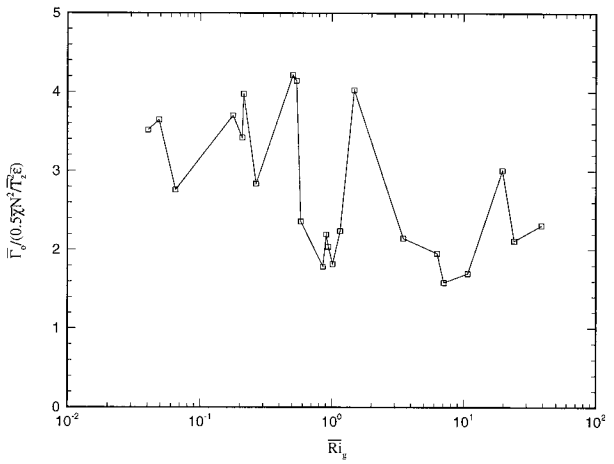

FIG. 10. Dissipation flux coefficient ratio $\overline{\Gamma}_o/\overline{\Gamma}_F$ vs $\overline{\mathrm{Ri}}_g$.

oceanic measurements encounter a similar condition when attempting to estimate the dissipation rate of mean-square temperature fluctuations.

c. *Measurements and parameterizations of eddy coefficients*

Below, the laboratory measurements of eddy diffusivities in stratified shear layers are compared with those of ocean, in particular, in the equatorial undercurrent where turbulent mixing is believed to be dominated by shear-induced turbulence (see Polzin 1996; Toole and Schmitt 1987; Sun et al. 1998). Since the eddy diffusivity parameterizations of Pacanowski and Philander (1981), namely,

$$K_m = \frac{\nu_o}{(1 + \alpha \mathrm{Ri}_g)^n} + \nu_b \tag{3.13}$$

and

$$K_\rho = \frac{K_m}{(1 + \alpha \mathrm{Ri}_g)} + \kappa_b, \tag{3.14}$$

where α, n, ν_o, ν_b, and κ_b are constants and Ri_g is the local gradient Richardson number, has been developed based on EUC observation, the data also can be compared with their parameterization.

Figures 11a and 11b show the dimensional form of the eddy coefficients together with those obtained in EUC by Peters et al. (1988), Moum and Osborn (1986), and Peters et al. (1995). Based on the assumption $K_\rho = K_T$, where K_T is the eddy diffusivity of heat, the parameterization of Peters et al. (1988) suggests the following:

$$K_m = 5.6x10^{-4} \cdot \mathrm{Ri}_g^{-8.2} \tag{3.15}$$

and

$$K_\rho = 3.0x10^{-5} \cdot \mathrm{Ri}_g^{-9.6} \tag{3.16}$$

for $\mathrm{Ri}_g \leq 0.25$ (where eddy coefficients have the units $m^2\ s^{-1}$) and

$$K_m = \frac{5.0}{(1.0 + 5.0\mathrm{Ri}_g)^{1.5}} + 0.2 \tag{3.17}$$

and

$$K_\rho = \frac{5.0}{(1.0 + 5.0\mathrm{Ri}_g)^{2.5}} + 0.01 \tag{3.18}$$

for $\mathrm{Ri}_g > 0.25$. Although it is recognized that the dimensional form of eddy coefficients are not the appropriate way of presenting data, given the vast differences between oceanic and laboratory conditions, Figs. 11a and 11b are presented to show the magnitudes of fluxes measured under different conditions, since ocean data is traditionally presented in dimensional form. It is interesting to note that laboratory $\overline{K}_\rho$ and $\overline{K}_m$ tend to drop to their molecular diffusivity levels (10^{-5} and 10^{-2} $cm^2\ s^{-1}$) at large $\overline{\mathrm{Ri}}_g$, indicating purely molecular transport of density and momentum at $\overline{\mathrm{Ri}}_g \simeq 15$ or so. Based on visualization studies of stratified shear layers, Narimousa et al. (1986) and Narimousa and Fernando (1988) have proposed that buoyancy transport across stratified shear layers becomes purely molecular diffusion dominated at this point.

In Pacanowski and Philander (1981), in consonance with the measurements taken during the mixed layer observations of EUC, the constants α, n, ν_o, ν_b, and κ_b were set to 5, 2, 100 $cm^2\ s^{-1}$, 1 $cm^2\ s^{-1}$, and 0.1 $cm^2\ s^{-1}$, respectively; these values were used in constructing Figs. 11 and 14–17. Also note that the data in Figs. 11a and 11b are based on vertically integrated quantities, namely

$$\overline{K}_m = \frac{\langle P \rangle}{\langle S \rangle^2} \tag{3.19}$$

and

$$\overline{K}_\rho = \frac{\langle B \rangle}{\langle N^2 \rangle}. \tag{3.20}$$

Figures 12a and 12b present the local estimations of eddy diffusivities for momentum K_m and density K_ρ, respectively. Both diffusivities are normalized by the shear layer thickness δ_s and velocity jump ΔU (recall the governing variables identified in section 1) and are plotted across the stratified shear layer, where ξ/δ_s is the normalized vertical location ($\xi/\delta_s = 0$ is the bottom of the shear layer). The variation of the diffusivities K_m and K_ρ follow strongly with that of the Reynolds stress ($u'w'$) and the buoyancy flux ($b'w'$), respectively (for both cases, the second-order correlations tend to decay faster than the respective mean gradients). Hence, they both exhibit peaks at or just above the center of the stratified shear layer.

In all laboratory measurements of turbulent diffusivities, experiments were performed only for the two-layer case; that is, $N = 0$ in the quiescent layer below the sharp pycnocline. The primary reason for limiting this set of measurements was due to the intrusive nature of the probe. As discussed in section 2, the vertical momentum and density fluxes were measured using a two-component (u, w) X-type hotfilm coupled with a mi-

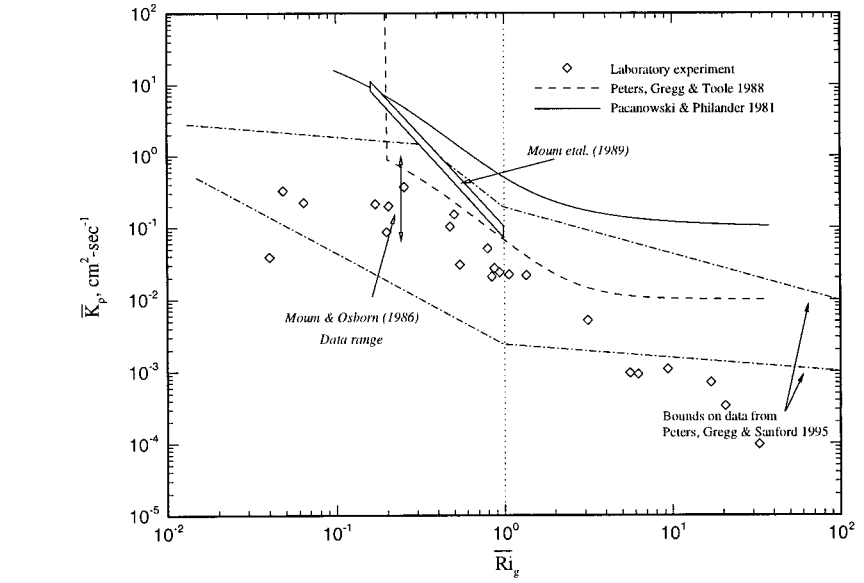

a.

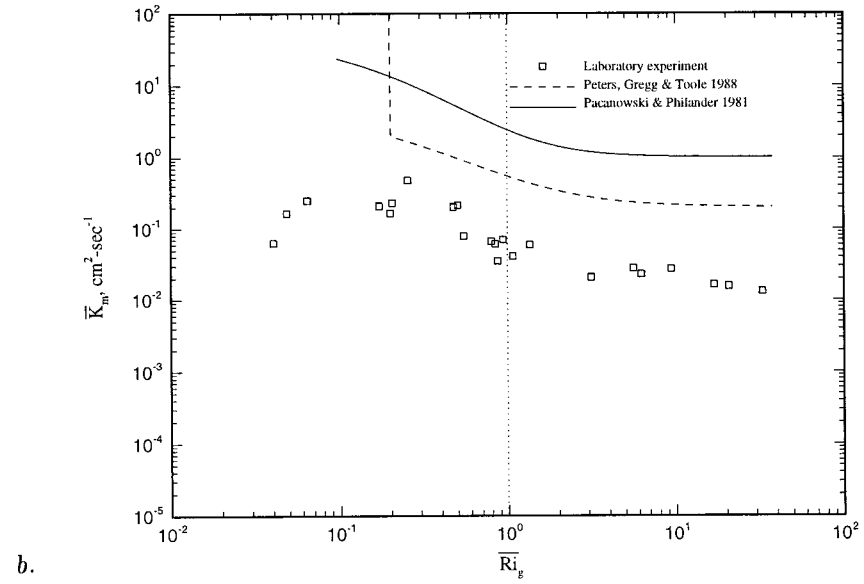

b.

FIG. 11. (a) Dimensional form of eddy diffusivity for density $\overline{K}_\rho$ plotted vs $\overline{\mathrm{Ri}}_g$ for the stratified shear layer. The solid line indicates the model proposed by Pacanowski and Philander (1981). The dashed line indicates the model proposed by Peters et al. (1988). The dashed–dotted line shows the bounds on data reported in Peters et al. (1995) from measurements taken in the Pacific Equatorial Undercurrent at 0°, 140°W in April 1987; (b) dimensional form of eddy diffusivity for momentum $\overline{K}_m$ plotted vs $\overline{\mathrm{Ri}}_g$. The solid line indicates the model proposed by Pacanowski and Philander (1981). The dashed line indicates the model proposed by Peters et al. (1988).

croscale conductivity probe. The physical intrusion of such probes can alter significantly the radiation of internal wave energy into the deep layer if it is stratified. However, measurements of the interfacial buoyancy flux via an alternative nonintrusive technique, laser-induced fluorescence (see SF01) were performed for both the two-layer case and the linearly stratified deep-layer case. It was determined that there exists a range of $\overline{\mathrm{Ri}}_g$ (i.e., $0.36 < \overline{\mathrm{Ri}}_g < 1.0$) where the deep layer stratification substantially reduces the vertical density flux due to the loss of energy to downward radiating internal waves. Outside of this parameter range, the influence of internal wave radiation is negligible. Therefore, when the data is properly normalized, it is likely that the laboratory

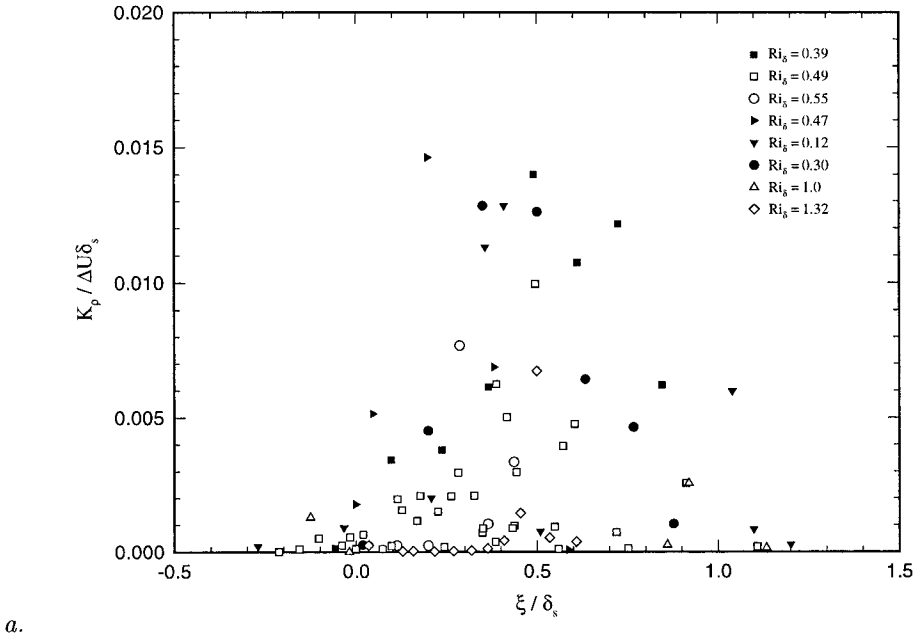

a.

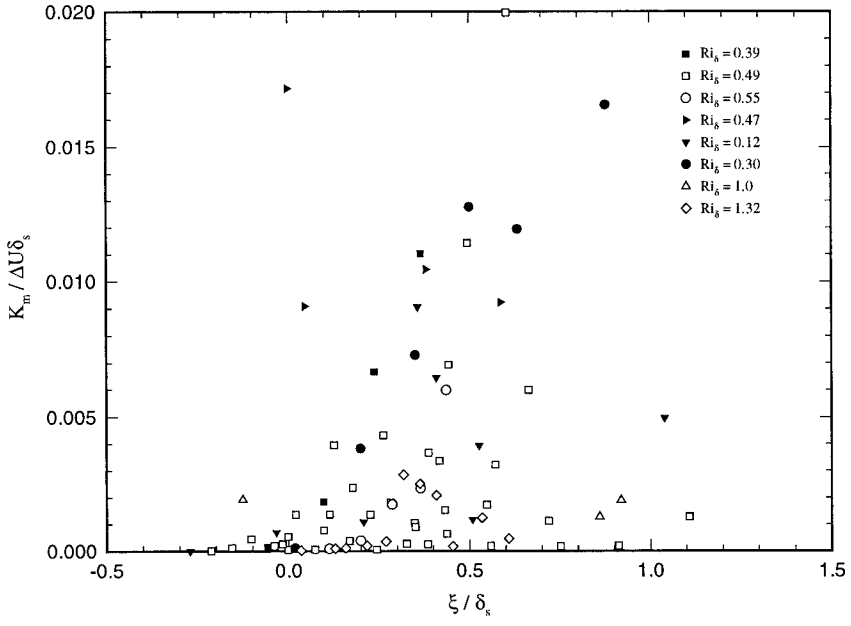

b.

FIG. 12. (a) Vertical profile of "local" eddy diffusivity for density K_ρ normalized by the shear layer properties, and (b) vertical profile of the eddy diffusivity for momentum K_m normalized by the shear layer properties.

results will overpredict the diffusivities of the continuously stratified oceanic case in the parameter range given above.

It is instructive to present laboratory data in a nondimensional form that has general validity to oceanic and other simulated shear layers. In section 1, the important governing variables for the laboratory problem were identified as ΔU, Δb, δ_s, δ_b, and some profile factor Π, which led to the identification of $\overline{\mathrm{Ri}}_g$ as a primary governing variable. In the laboratory problem, all of the above variables are dependent on $\overline{\mathrm{Ri}}_g$, but in oceans other variables may play a role, which should reflect from observables such as velocity and density profiles. Careful inspection, however, reveals that there are striking similarities between velocity and density profiles of oceanic and laboratory layers.

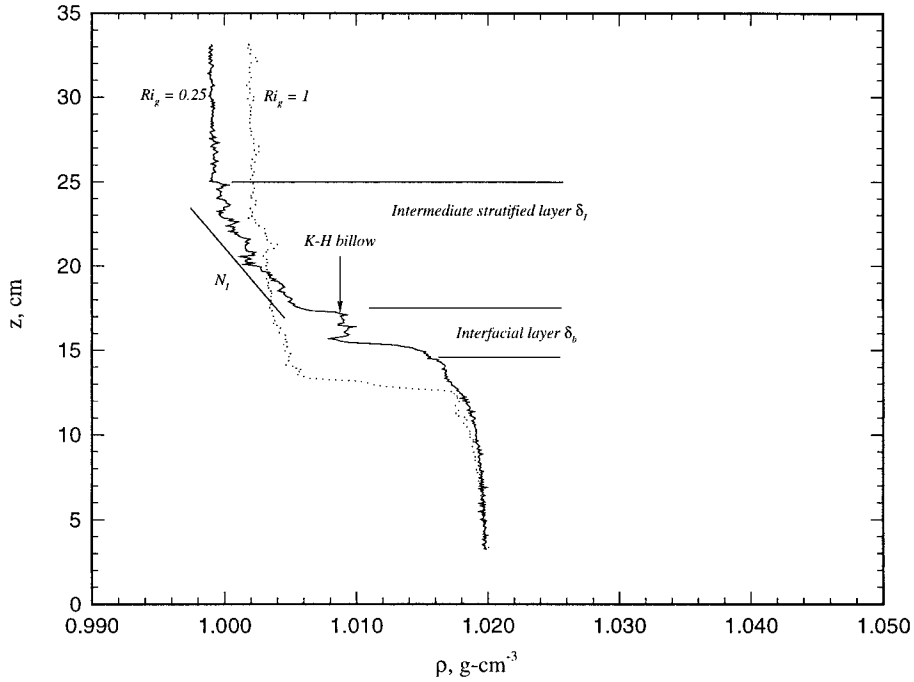

FIG. 13. Vertical profiles of the density during experiments with the two-layer case.

In particular, the structure of the density stratification is quite similar. In the experiments reported herein, the density stratification generally extends beyond the strongly stratified and permanent interfacial layer (of scale δ_b) well into the mixed layer (of depth D) over a scale δ_I. This latter scale arises due to local mixing generated by the breaking of instabilities, and hence this region is highly time varying. The scale of the density stratification can be defined to be the sum of the two scales $\Delta_b \approx \delta_b + \delta_I$ when the deep layer is not stratified; that is, $N = 0$. Figure 13 presents several density profiles for different values of the mean gradient Richardson number ($\overline{\mathrm{Ri}}_g$) measured at the base of the mixed layer. A typical profile (i.e., $\overline{\mathrm{Ri}}_g < 1$) has four distinct layers: an interfacial layer of thickness δ_b above which lies an intermediate stratified layer of thickness δ_I (which is equivalent to ''thermostads'' in oceans), both bounded by a mixed layer above and a homogeneous layer below (the uppermost and lowermost layers are of scale D). The region combining the intermediate and interfacial layers (i.e., Δ_b) exhibits the strongest shear (across which $\Delta U = \Delta U_b$ occurs). The intermediate layer gradually decreases with increasing $\overline{\mathrm{Ri}}_g$ and virtually disappears at $\overline{\mathrm{Ri}}_g > 1$.

Following the above definitions of various layers, one can identify similar layers in the ocean density structure shown in Figs. 5 and 6 of Moum et al. (1989) (see Fig. 2 of this paper). In particular, the primary interfacial layer of thickness δ_b extends approximately from 90 to 130 m depth (with a temperature gradient 0.137°C/m), below which exists a quiescent, weakly stratified deep layer ($h > 130$ m) and above which is a slightly weaker stratified layer of thickness δ_I extending from 30 to 90 m depth (with a temperature gradient of 0.036°C/m). The difference in the density gradient is almost a factor of 4 between the two layers, comparing well with the laboratory experiment. In the oceanic data, a shear layer extends vertically from 20 to 150 m depth, bounding the entire vertical range of the density stratification in the interfacial and intermediate layers. The strength of shear across this layer of thickness $\delta_s \sim 130$ m is approximately 0.02 s^{-1} except for a thin layer extending from 100 to 120 m depth. The mean gradient Richardson number calculated with a 10-m resolution appears to be approximately 0.4–0.45. To contrast these scales with those in the laboratory, we compare several scales extracted from both sets of data for approximately the same mean gradient Richardson number $\overline{\mathrm{Ri}}_g \sim 0.4 - 0.45$. The scales used for comparison include the interfacial thickness δ_b [1.9 cm: SF01; 40 m (90 to 130 m): Moum et al. (1989)], the intermediate layer thickness δ_I [3.4 cm; 60 m (30 to 90 m)], the entire stratified layer thickness Δ_b [5.3 cm; 100 m (30 to 130 m)], the scale across which Ri_g varies δ_{Ri} [3.1 cm; 25 m (85 to 110 m)], and the shear layer thickness δ_s [6.1 cm; 120 m (30 to 150 m)]. Here the Ri_g scale was calculated by obtaining Ri_g profiles, as shown in Fig. 1b; δ_{Ri} represents the distance between the respective points in the upper and lower layers where $\overline{\mathrm{Ri}}_g$ fell to 5% its peak value (since $\delta_{\mathrm{Ri}} \simeq \delta_s$; the shear layer thickness δ_s was employed for measurements when $\overline{\mathrm{Ri}}_g < 1$, where $\overline{\mathrm{Ri}}_g$ profiles were not obtained). Note that 1 cm in the laboratory is on the order of 10 m in the ocean.

Using the above ΔU_b and Δ_b values of Moum et al.

(1989), the EUC measurements of Peters et al. (1988) and the semiempirical parameterizations of Pacanowski and Philander (1981) for K_m and K_ρ were normalized. These results together with the corresponding normalized values of the present measurements shown in Figs. 11a and 11b are shown in Figs. 14a and 14b. For all $\overline{\mathrm{Ri}}_g$, the laboratory measurements of $\overline{K}_\rho$ exceed the oceanic values and those used in empirical models, sometimes by almost an order of magnitude. This can be, in part, due to the lack of vertical resolution in the oceanic

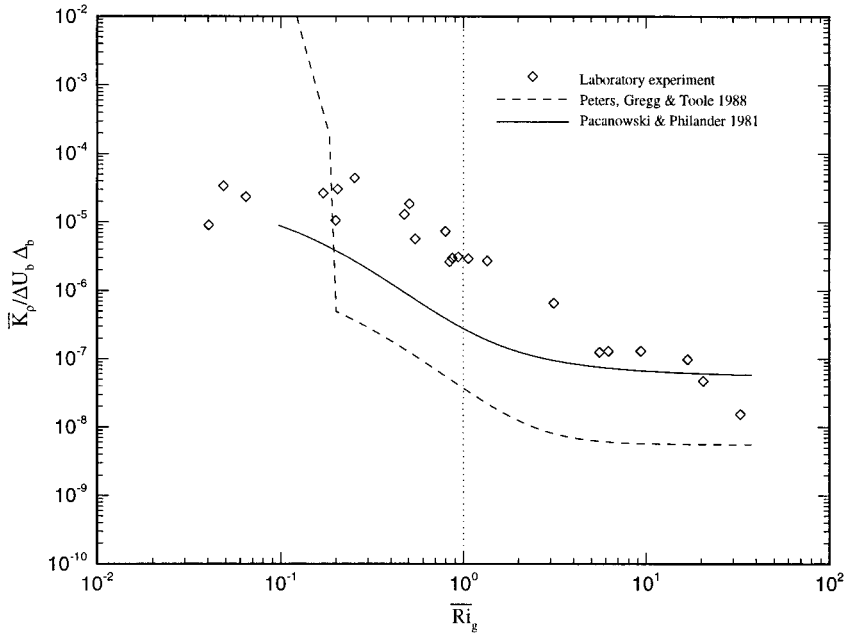

a.

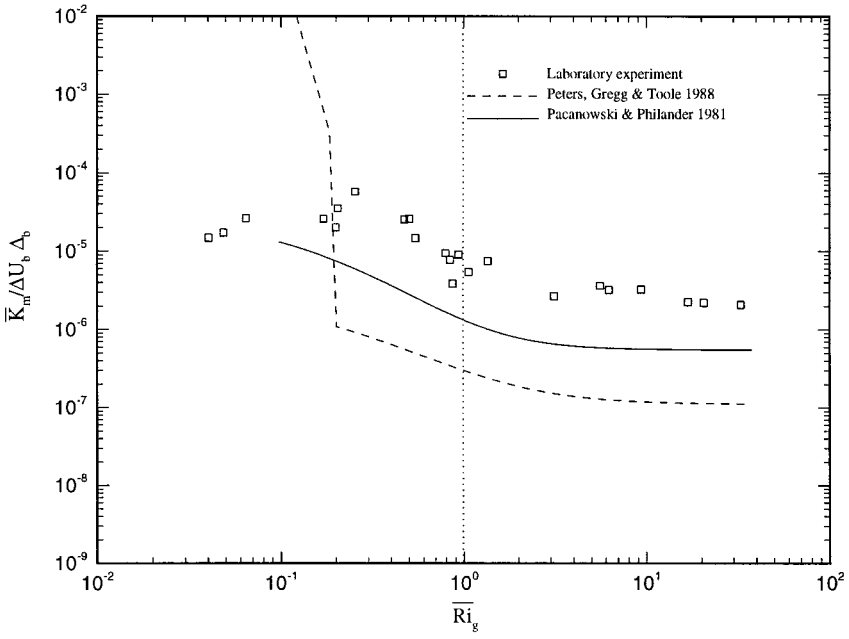

b.

FIG. 14. (a) The eddy diffusivity for density $\overline{K}_\rho$ normalized using the stratified layer thickness Δ_b and the corresponding velocity difference across that layer ΔU_b plotted vs $\overline{\mathrm{Ri}}_g$; (b) the eddy diffusivity for momentum $\overline{K}_m$ normalized using Δ_b and ΔU_b plotted vs $\overline{\mathrm{Ri}}_g$. The solid line indicates the model proposed by Pacanowski and Philander (1981). The dashed line indicates the model proposed by Peters et al. (1988).

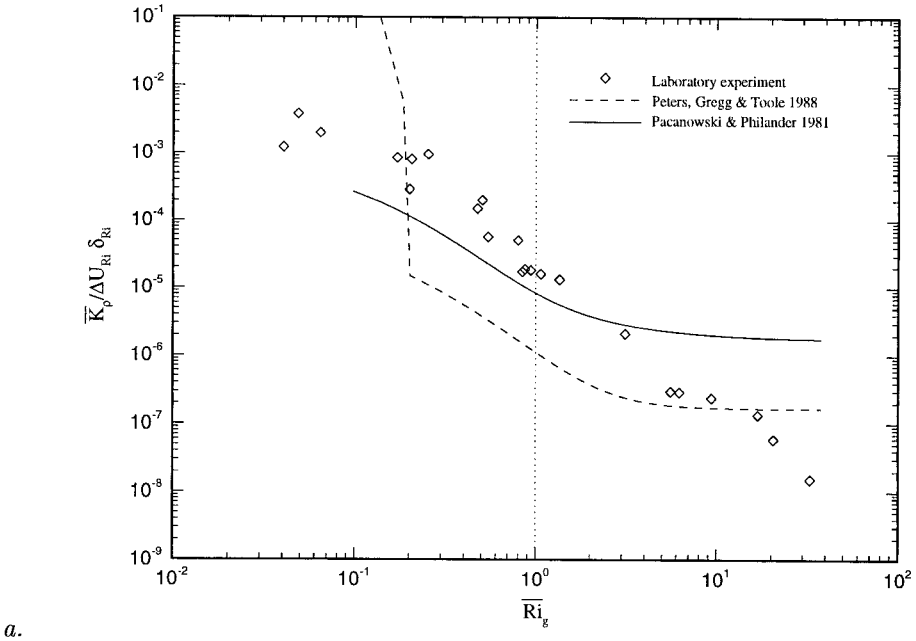

a.

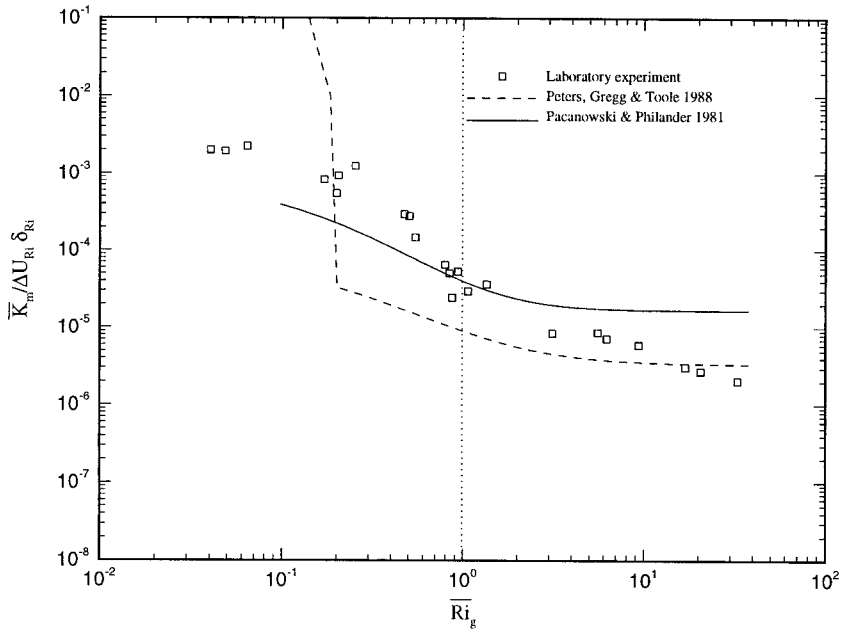

b.

FIG. 15. (a) The eddy diffusivity for density $\overline{K}_\rho$ normalized using the layer thickness across which the gradient Richardson number varies δ_{Ri} and the corresponding velocity difference across that layer ΔU_{Ri} plotted vs $\overline{Ri}_g$; (b) the eddy diffusivity for momentum $\overline{K}_m$ normalized using the layer thickness across which the gradient Richardson number varies δ_{Ri} and the corresponding velocity difference across that layer ΔU_{Ri} plotted vs $\overline{Ri}_g$.

observations and, more importantly, due to the intricacy of oceanic measurements. The same conclusion can be drawn from the measurement of $\overline{K}_m$, as shown in Fig. 14b. It is, however, interesting that the shapes of the diffusivity-$\overline{Ri}_g$ curves for both density and momentum are similar to those predicted by the parameterization schemes, in particular, for $\overline{Ri}_g > 1$. This holds true at lower $\overline{Ri}_g$ when compared with the formulation of Pacanowski and Philander (1981).

In Figs. 15a and 15b, the data of Figs. 11a and 11b are renormalized using the shear layer scales (across which $\overline{Ri}_g$ varies). The agreement between the labora-

tory and oceanic data/parameterizations is much improved in this case, especially with the parameterizations proposed by Pacanowski and Philander (1981). This is understandable given the nature of the integrated energy budget considered in laboratory measurements. Since the fluxes were averaged over the entire region where stratified mixing is significant (which is of the order of δ_s or δ_{Ri}), scales based on velocity (ΔU) and Ri_g variation in that region are expected to perform best. On the same token, the Pacanowski and Philander (1981) scheme has been developed based on an overall comparison between EUC structure and computer simulations, and hence the parameterizations so developed are bulk representation over a certain computational region (grid cell).

Lastly, Figs. 16a and 16b present a third normalization of the data presented in Figs. 11a and 11b. Therein, the eddy coefficients for mass $\overline{K}_\rho$ and momentum $\overline{K}_m$ were normalized by the Ozmidov length scale L_o^* and the respective velocity difference ΔU_o associated with the evaluation of L_o^*. For the laboratory experiment, the Ozmidov scale was evaluated from the layer-averaged quantities; that is, $L_o^* = (\langle\epsilon\rangle/\langle N\rangle^3)^{1/2}$. Therefore, the respective velocity scale ΔU_o was chosen to be the distance between the integration limits (i.e., $\Delta U_o \simeq \Delta U_{\delta_s}$). For the ocean data, a single Ozmidov length scale and corresponding velocity scale were chosen. From Moum (1996b), the Ozmidov length scale is reported to be approximately 1 m in the thermocline, and this appears to be consistent with the data presented in Figs. 5 and 6 of Moum et al. (1989). In Moum et al. (1989), the Ozmidov length scale was estimated to be $L_o^* \simeq 4.3$ m ($N \sim 5$ cph, $\epsilon \sim 5 \times 10^{-8}$ m^2 s^{-1}, and $\mathrm{Ri}_g \sim 0.25$) for a range in depth of 30 to 90 m (oceanic intermediate layer), whereas it was approximately $L_o^* \simeq 0.2$ m, ($N \sim 10$ cph, $\epsilon \sim 5 \times 10^{-10}$ m^2 s^{-1}, and $\mathrm{Ri}_g \sim 1$) for 90 to 130 m. A layer-averaged value for the entire density stratified layer (i.e., 30 to 130 m) was determined to be approximately 1 to 3 m depending upon the value of the TKE dissipation (i.e., $\epsilon \sim 10^{-7} - 10^{-8}$ m^2 s^{-1} given $N \sim 7.5$ cph). Since the above estimated values are of order $L_o^* \sim 1$ m, a length scale of 1 m and a respective velocity scale of $\Delta U_o \sim (d\overline{U}/dz)L_o^* = 0.01$ m s^{-1} (corresponding to a value of the mean vertical shear of 0.01 s^{-1} from Fig. 5 in Moum et al. 1989). As evident from Figs. 16a and 16b, the laboratory data appear to agree very well with the oceanic parameterizations of Pacanowski and Philander (1981) for both $\overline{K}_\rho$ and $\overline{K}_m$.

Figure 17 shows the dependence of $\overline{K}_\rho/\overline{K}_m$ on $\overline{\mathrm{Ri}}_g$. It is clear that at low stratifications/strong shear, $\overline{\mathrm{Ri}}_g < 1$ (predominantly K–H activity), $\overline{K}_\rho/\overline{K}_m$ does not depend significantly on $\overline{\mathrm{Ri}}_g$, but thereafter, the diffusivity of momentum becomes significantly larger than the diffusivity of mass. This can be attributed to the generation of turbulence by intermittent breaking of waves, in particular Hölmböe waves (SF01), at $\overline{\mathrm{Ri}}_g > 1$. The extent of mixing caused by the instabilities of these waves is much smaller (due to their intermittent breaking) than those of K–H instabilities, although these waves transfer appreciable momentum.

The general agreement between the laboratory measurements and the parameterizations of Pacanowski and Philander (1981) and Peters et al. (1988) for $\overline{\mathrm{Ri}}_g < 1$ or so is reasonable, but for $\overline{\mathrm{Ri}}_g > 3.8$ or so, Pacanowski and Philander (1981) overpredicts $\overline{K}_\rho/\overline{K}_m$ whereas Peters et al. (1988) shows a good agreement with the laboratory data. As expected, at $\overline{\mathrm{Ri}}_g > 15$, molecular diffusion controls buoyancy transport and $\overline{K}_\rho/\overline{K}_m$ drops toward the corresponding molecular diffusivity ratio.

4. Summary and conclusions

Point measurements of the buoyancy flux $\overline{b'w'}$ (or B), shear production of turbulent kinetic energy P, and the turbulent kinetic energy dissipation ϵ were made over a two-dimensional swath of a stratified shear layer, which were integrated over the shear layer thickness to obtain their averaged values $\langle B\rangle$, $\langle P\rangle$, and $\langle\epsilon\rangle$, respectively. Given the horizontal homogeneity, these averages are representative of three-dimensional volume averages. The results showed that the flux Richardson number $\overline{\mathrm{Ri}}_f$, the flux dissipation coefficient $\overline{\Gamma}_o$, and the eddy diffusivities of momentum $\overline{K}_m$ and density $\overline{K}_\rho$ are directly related to a characteristic Richardson number, that is, the gradient Richardson number $\overline{\mathrm{Ri}}_g$ at the top of the density interface, which was approximately equal to the $\overline{\mathrm{Ri}}_g$ averaged over the shear layer). The mixing mechanism at the interface also was found to be determined by $\overline{\mathrm{Ri}}_g$. The mixing is governed by pure K–H waves from $0.086 < \overline{\mathrm{Ri}}_g < 0.36$ and K–H and asymmetric waves from $0.36 < \overline{\mathrm{Ri}}_g < 1$, in which regions $\overline{\mathrm{Ri}}_f$ and $\overline{\Gamma}_o$ increase with $\overline{\mathrm{Ri}}_g$. Beyond $\overline{\mathrm{Ri}}_g > 1$, mixing is governed by asymmetric waves from $1 < \overline{\mathrm{Ri}}_g < 1.3$ and symmetric Hölmböe waves from $\overline{\mathrm{Ri}}_g > 1.3$; in this $\overline{\mathrm{Ri}}_g$ range, $\overline{\mathrm{Ri}}_f$ and $\overline{\Gamma}_o$ decrease with increasing $\overline{\mathrm{Ri}}_g$. At $\overline{\mathrm{Ri}}_g \sim 1$, $\overline{\mathrm{Ri}}_f$ peaks at a value of approximately 0.4. Comparisons of laboratory-based Ri_f versus Ri_g curves with those proposed by the Mellor and Yamada (1974) level 2 turbulent closure model showed only a slight agreement in that the level 2 model predicts a constant $\overline{\mathrm{Ri}}_f$ beyond $\overline{\mathrm{Ri}}_g > 1$.

The K–H regime can be partitioned into two subregimes. When $\overline{\mathrm{Ri}}_g < 0.36$, the existance of pure K–H waves in the shear layer is weakly affected by the stratification, $\overline{\mathrm{Ri}}_f (\sim 0.08)$ and $\overline{\Gamma} (\sim 0.1)$ are small, and the turbulent eddy transport coefficients are constants and equal ($\overline{K}_m/\Delta U_b \Delta_b \sim \overline{K}_\rho/\Delta U_b \Delta_b \sim 2 \times 10^{-5}$), and the mixing properties are fairly independent of the Richardson number. When $0.36 < \overline{\mathrm{Ri}}_g < 1$, $\overline{\mathrm{Ri}}_f$ and $\overline{\Gamma}$ sharply increase with the Richardson number, peaking ($\overline{\mathrm{Ri}}_f \sim 0.4$ and $\overline{\Gamma} \sim 0.65$) at $\overline{\mathrm{Ri}}_g \sim 1$ whence the K–H regime subsides, paving the way to purely asymmetric waves. The diffusivities $\overline{K}_m/\Delta U \Delta_b$ and $\overline{K}_\rho/\Delta U \Delta_b$ show a decrease in this regime, though $\overline{K}_\rho/\overline{K}_m$ still remains order unity. This result shows that the transports of density and momentum are dominated by turbulent mixing,

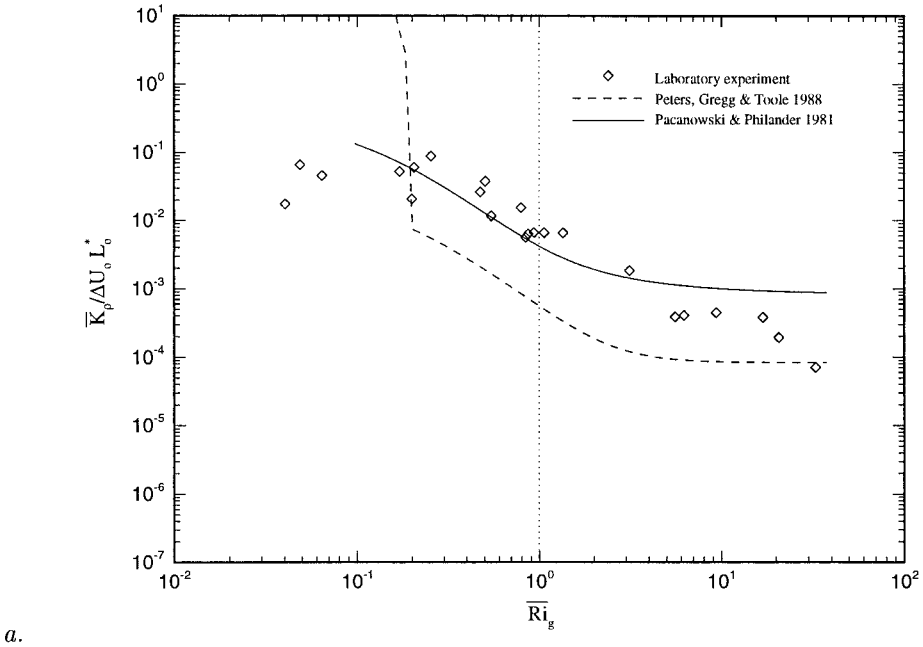

a.

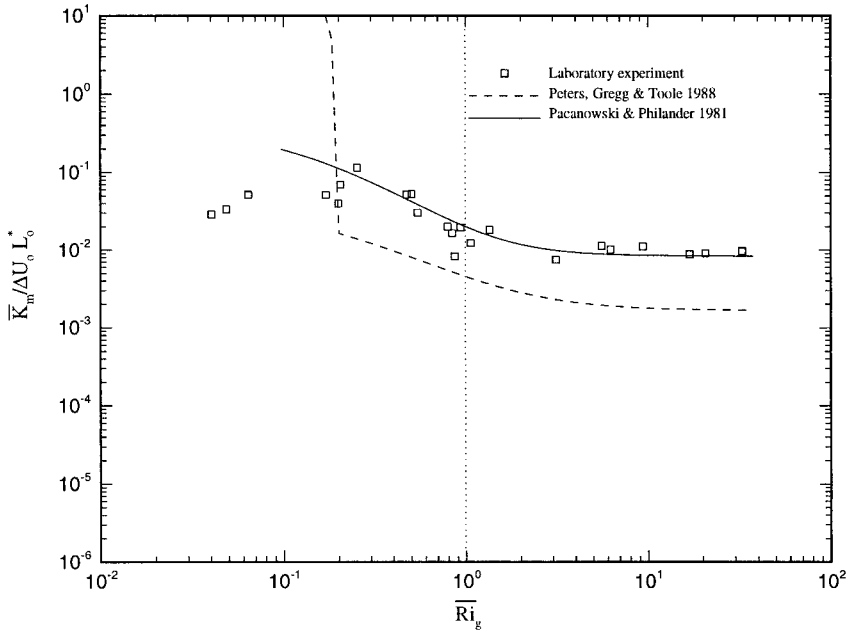

b.

FIG. 16. (a) The eddy diffusivity for density $\overline{K}_\rho$ normalized using the Ozmidov scale L_o^* and the corresponding velocity difference across that layer ΔU_o plotted vs $\overline{\mathrm{Ri}}_g$; (b) the eddy diffusivity for momentum $\overline{K}_m$ normalized using the Ozmidov scale L_o^* and the corresponding velocity difference across that layer ΔU_o plotted vs $\overline{\mathrm{Ri}}_g$.

rather than by internal waves wherein momentum is transported much more efficiently compared to the mass transport. The latter is the scenario occurring in the wave breaking regime, $\overline{\mathrm{Ri}}_g > 1$, where the strong intermittency in the shear layer and its decrease with the Richardson number causes $\overline{\mathrm{Ri}}_f$ and $\overline{\Gamma}_o$ to sharply drop with $\overline{\mathrm{Ri}}_g$. This drop is also evident in the diffusivity measurements, which show a distinct drop of $\overline{K}_m$ and $\overline{K}_\rho$ beyond $\overline{\mathrm{Ri}}_g \sim 1$, finally achieving their corresponding molecular values at $\overline{\mathrm{Ri}}_g > 15$.

The measurements were used to validate some commonly used oceanic flux and diffusivity parameteriza-

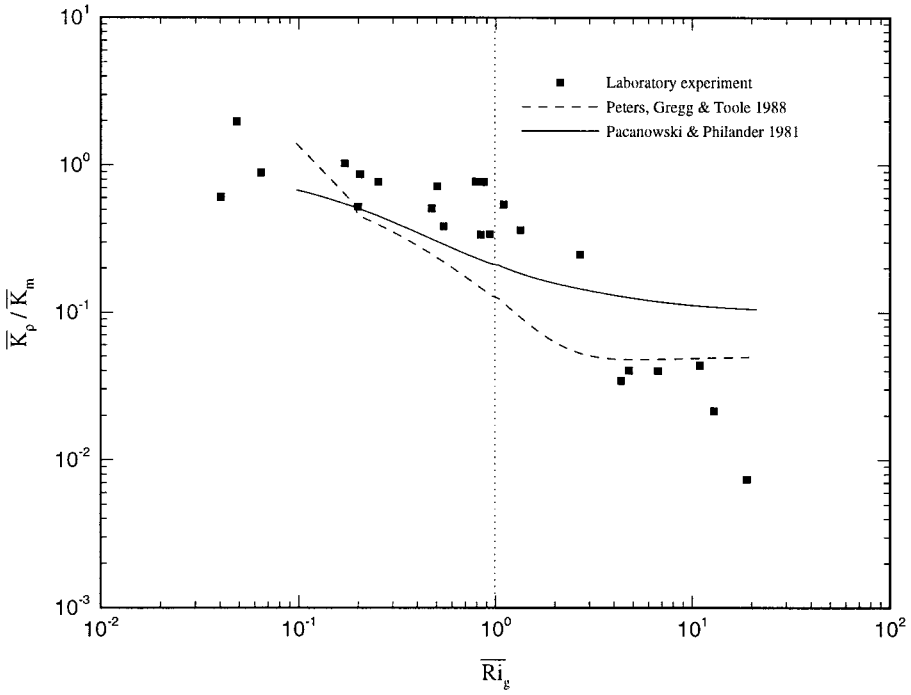

FIG. 17. The ratio of eddy diffusivities $\overline{K}_\rho/\overline{K}_m$ plotted vs $\overline{\mathrm{Ri}}_g$ for the stratified shear layer. The solid line indicates the ratio proposed by Pacanowski and Philander (1981). The dashed line indicates the ratio proposed by Peters et al. (1988).

tions. It was shown that the Osborn (1980) formula can be satisfactorily used to estimate the buoyancy flux and the eddy diffusivity K_ρ when the dependence of $\overline{\mathrm{Ri}}_f$ and $\overline{\Gamma}_o$ on the Richardson number is properly accounted.

As a result of the variation of $\overline{\mathrm{Ri}}_f$ in the range $0.05 < \overline{\mathrm{Ri}}_f < 0.4$, the dissipation flux coefficient $\overline{\Gamma}_o$ was found to vary between 0.06 and 0.65. This is in reasonable agreement with the results of Moum et al. (1989), which indicated a range of 0.12 to 0.48. Therefore, an improvement to the method of estimating K_ρ using the Osborn model can be derived from these measurements by considering the dependence of $\overline{\mathrm{Ri}}_f$ with $\overline{\mathrm{Ri}}_g$. It was also shown that the estimation of the flux dissipation coefficient using scalar dissipation rates (Γ_F) tended to underpredict values (Γ_o) estimated using the direct measurement of the buoyancy flux and turbulent kinetic energy dissipation rate by as much as a factor of 3. One possible explanation for this discrepancy may be the lack of observance of a $k^{-5/3}$ spectrum, in particular, where the buoyancy flux is greatest (at the edge of the interfacial layer). Due to a poor fit to the spectra in this region, the value of $\overline{\chi}$ could have been consistently underestimated in the laboratory experiments.

Estimation of the coefficients of eddy diffusivity for density $\overline{K}_\rho$ and momentum $\overline{K}_m$ were made in the laboratory stratified shear layer. Comparison of these measurements with oceanic numerical-model closure schemes (i.e., Pacanowski and Philander 1981; Peters et al. 1988) showed that the laboratory values can be an order of magnitude greater when scaled by the thickness of the density-stratified layer and the corresponding velocity difference across that layer. Similarly, there was only a fair agreement with diffusivities derived from oceanic microstructure measurements. However, when the data were scaled by the length scale over which the Richardson number varies across the shear layer (which was approximately equal to the shear layer thickness in the laboratory experiment) and corresponding velocity scale, good agreement was achieved. This agreement was further improved when the eddy coefficients were scaled using the Ozmidov scale and an appropriate velocity scale. The dependence of the measured diffusivity ratio $\overline{K}_\rho/\overline{K}_m$ was in fair agreement with the parameterizations of Pacanowski and Philander (1981) and Peters et al. (1988).

Acknowledgments. Stratified turbulent shear flow research within the Environmental Fluid Dynamics Laboratory at Arizona State University is sponsored by the Office of Naval Research (Physical Oceanography Program), the Army Research Office, and the National Science Foundation. The authors wish to gratefully acknowledge this support. Furthermore, we wish to thank Dr. Chang Y. Ching, Professor Eliezer Kit, and Mr. Leonard Montenegro for their endless technical support. Lastly, the authors wish to thank the referees for their insightful comments that have led to substantial changes to the manuscript.

REFERENCES

Abarbanel, H. D. I., D. D. Holm, J. E. Marsden, and T. Ratiu, 1986: Effect of variation in density on the stability of superposed streams. *Trans. Roy. Soc. London,* **318,** 349–409.

Chereskin, T. K., J. N. Moum, P. J. Stabeno, D. R. Caldwell, C. A. Paulson, L. A. Regier, and D. Halpern, 1986: Fine-scale variability at 140 W in the equatorial Pacific. *J. Geophys. Res.*, **91,** 12 887–12 897.

Corrsin, S., 1951: On the spectrum of isotropic temperature fluctuations in isotropic turbulence. *J. Appl. Phys.*, **22,** 469–473.

Desaubies, Y., and W. K. Smith, 1982: Statistics of Richardson number and instability in oceanic internal waves. *J. Phys. Oceanogr.*, **12,** 1245–1259.

De Silva, I. P. D., 1991: Studies of turbulent mixing in stratified turbulent patches. Ph.D. thesis, Arizona State University, 212 pp.

——, L. Montenegro, and H. J. S. Fernando, 1990: Measurement of interfacial distortions at a stratified entrainment interface. *Exp. Fluids,* **9,** 174–177.

——, H. J. S. Fernando, F. Eaton, and D. Hebert, 1996: Evolution of Kelvin–Helmholtz billows in nature and laboratory. *Earth Planet. Sci. Lett.,* **143,** 217–231.

——, A. Brandt, L. Montenegro, and H. J. S. Fernando, 1999: Gradient Richardson number measurements in a stratified shear layer. *Dyn. Atmos. Oceans,* **30,** 47–63.

Eriksen, C. C., 1978: Measurements and models of fine structure, internal gravity waves and breaking in the deep ocean. *J. Geophys. Res.*, **83** (C6), 2989–3009.

——, 1985: The Tropic Heat Program: An overview. *Eos, Trans. Amer. Geophys. Union,* **66,** 50–52.

Gargett, A. E., and J. N. Moum, 1995: Mixing efficiencies in turbulent tidal fronts: Results from direct and indirect measurements of the density flux. *J. Geophys. Res.*, **81,** 1180–1196.

——, T. R. Osborn, and P. W. Nasmyth, 1984: Local isotropy and the decay of turbulence in a stratified fluid. *J. Fluid Mech.*, **144,** 231–280.

Gregg, M. C., 1976: Temperature and salinity microstructure in the Pacific Equatorial Under-current. *J. Geophys. Res.*, **81,** 1180–1196.

——, H. Peters, J. C. Wesson, N. S. Oakey, and T. J. Shay, 1985: Intensive measurements of turbulence and shear in the equatorial undercurrent. *Nature,* **318,** 140–144.

Halpern, D., 1976: Structure of coastal upwelling event observed off Oregon during July 1973. *Deep-Sea Res.*, **23,** 495–508.

Hebert, D., J. N. Moum, C. A. Paulson, and D. R. Caldwell, 1992: Turbulence and internal waves at the equator. Part II: Details of a single event. *J. Phys. Oceanogr.,* **22,** 1346–1356.

Itsweire, E. C., J. R. Koseff, D. A. Briggs, and J. H. Ferziger, 1993: Turbulence in stratified shear flows: Implications for interpreting shear-induced mixing in the ocean. *J. Phys. Oceanogr.,* **23,** 1508–1522.

Ivey, G. N., and J. Imberger, 1991: On the nature of turbulence in a stratified fluid. Part I: The energetics of mixing. *J. Phys. Oceanogr.*, **21,** 650–658.

Killworth, P., 1998: Something stirs in the deep. *Nature,* **396,** 720–721.

Kundu, P. K., and R. C. Beardsley, 1991: Evidence of a critical Richardson number in moored measurements during the upwelling season off Northern California. *J. Geophys. Res.*, **96,** 4855–4868.

Kunze, E., A. J. Williams III, and M. G. Briscoe, 1990: Observations of shear and vertical stability from neutrally buoyant float. *J. Geophys. Res.*, **95** (C10), 18 127–18 142.

Lawrence, G. A., F. K. Browand, and L. G. Redekopp, 1991: The stability of a sheared density interface. *Phys. Fluids A,* **3,** 2360–2370.

Majda, A., and M. G. Shefter, 1998: Elementary stratified flows with instability at large Richardson number. *J. Fluid. Mech.,* **376,** 319–350.

Mellor, G. L., and T. Yamada, 1974: A hierarchy of turbulence closure models for planetary boundary layers. *J. Atmos. Sci.,* **31,** 1791–1806.

——, and ——, 1982: Development of a turbulence closure model for geophysical fluid problems. *Rev. Geophys. Space Phys.,* **4,** 851–875.

Miles, J. W., 1986: Richardson's criterion for the stability of stratified shear flow. *Phys. Fluids,* **29,** 3470–3471.

Moum, J. N., 1996a: Efficiency of mixing in the main thermocline. *J. Geophys. Res.*, **101,** (C5), 12 057–12 069.

——, 1996b: Energy containing scales of turbulence in the ocean. *J. Geophys. Res.*, **101** (C6), 14 095–14 109.

——, and D. R. Caldwell, 1985: Local influences on shear-flow turbulence in the equatorial ocean. *Science,* **230,** 315–316.

——, and T. R. Osborn, 1986: Mixing in the main thermocline. *J. Phys. Oceanogr.,* **16,** 1250–1259.

——, ——, and C. A. Paulson, 1989: Mixing in the equatorial surface layer. *J. Geophys. Res.*, **94,** 2005–2021.

Narimousa, S., and H. J. S. Fernando, 1988: On the sheared density interface of an entraining stratified fluid. *J. Fluid Mech.*, **174,** 1–22.

——, R. R. Long, and S. A. Kitaigorodskii, 1986: Entrainment due to turbulent shear flow at the interface of a stably stratified fluid. *Tellus,* **38A,** 76–87.

Oboukhov, A. M., 1949: Structure of the temperature field in turbulent flows. *Izv. Akad. Nauk SSSR Geogr. Geophys.*, **13,** 58–62.

Odell, G. M., and L. S. G. Kovasznay, 1971: A new type of water channel with density stratification. *J. Fluid Mech.*, **50,** 535–543.

Osborn, T. R., 1980: Estimates of the local rate of vertical diffusion from dissipation measurements. *J. Phys. Oceanogr.*, **10,** 83–89.

——, and C. S. Cox, 1972: Oceanic fine structure. *Geophys. Fluid Dyn.,* **3,** 321–345.

Pacanowski, R. C., and S. G. H. Philander, 1981: Parameterization of vertical mixing in numerical models of tropical oceans. *J. Phys. Oceanogr.*, **11,** 1443–1451.

Peters, H., M. C. Gregg, and J. M. Toole, 1988: On the parameterization of equatorial turbulence. *J. Geophys. Res.*, **93** (C2), 1199–1218.

——, ——, and T. B. Sanford, 1995: On the parameterization of equatorial turbulence: Effect of fine-scale variations below the range of the diurnal cycle. *J. Geophys. Res.*, **100** (C9), 18 333–18 348.

Polzin, K., 1996: Statistics of the Richardson number: Mixing models and finestructure. *J. Phys. Oceanogr.*, **26,** 1409–1425.

Richardson, L. F., 1920: The supply of energy from and to atmospheric eddies. *Proc. Roy. Soc. London,* **97,** 354–373.

Stephenson, P. W., and H. J. S. Fernando, 1991: Turbulence and mixing in a stratified shear flow. *Geophys. Astrophys. Fluid Dyn.,* **59,** 147–164.

Strang, E. J., 1997: Entrainment and mixing in stratified shear flows. Ph.D. dissertation, Arizona State University, 219 pp.

——, and H. J. S. Fernando, 2001: Entrainment and mixing in stratified shear flows. *J. Fluid Mech.,* **428,** 349–386.

Sun, C., W. D. Smyth, and J. N. Moum, 1998: Dynamic instability of stratified shear flow in the upper equatorial Pacific. *J. Geophys. Res.,* **103,** 10 323–10 337.

Thompson, R. O. R. Y., 1984: Formation of thermoclines in zero-mean-shear turbulence. *J. Geophys. Res.,* **89,** 8017–8021.

Toole, J. M., and R. W. Schmitt, 1987: Small-scale structures in the Northwest Atlantic subtropical front. *Nature,* **327,** 47–49.

——, H. Peters, and M. C. Gregg, 1987: Upper ocean shear and density variability at the equator during Tropic Heat. *J. Phys. Oceanogr.,* **17,** 1397–1406.

Woods, J. D., 1968: Wave-induced shear instability in the summer thermocline. *J. Fluid Mech.,* **32,** 791–800.